Available online at www.sciencedirect.com
ScienceDirect
Journal of Sound and Vibration 320 (2009) 1039–1063
JOURNAL OF SOUND AND VIBRATION
www.elsevier.com/locate/jsvi

Impact of tooth friction and its bending effect on gear dynamics

Gang Liu, Robert G. Parker*

Department of Mechanical Engineering, The Ohio State University, 201 W. 19th Avenue, Columbus, OH 43210, USA

Received 23 May 2007; received in revised form 16 August 2008; accepted 20 August 2008
Handling Editor: S. Bolton
Available online 18 October 2008

Abstract

This work studies the influences of tooth friction on parametric instabilities and dynamic response of a single-mesh gear pair. A mechanism whereby tooth friction causes gear tooth bending is shown to significantly impact the dynamic response. A dynamic translational–rotational model is developed to consider this mechanism together with the other contributions of tooth friction and mesh stiffness fluctuation. An iterative integration method to analyze parametric instabilities is proposed and compared with an established numerical method. Perturbation analysis is conducted to find approximate solutions that predict and explain the numerical parametric instabilities. The effects of time-varying friction moments about the gear centers and friction-induced tooth bending are critical to parametric instabilities and dynamic response. The impacts of friction coefficient, bending effect, contact ratio, and modal damping on the stability boundaries are revealed. Finally, the friction bending effect on the nonlinear dynamic response is examined and validated by finite element results.

1. Introduction

In the various treatments of the gear mesh characteristics in the numerous mathematical gear models found in the literature [1–3], most models neglect the dynamic contribution of tooth friction compared with mesh forces normal to the tooth surface. Parametric excitation from variable mesh stiffness and geometric deviations of tooth surfaces are usually treated as the dominant sources of gear vibration [4,5]. Recently, tooth friction was demonstrated as an important factor in gear dynamics. Velex and Cahouet [6] analyze tooth friction in spur and helical gear dynamics. The comparison between simulated and measured bearing forces reveals the potentially significant contribution of tooth friction to gear vibration. The importance of tooth friction to structure-borne vibration of helical gear systems and to vibration reduction of gears with minimal static transmission error is discussed in Refs. [7,8]. Vaishya and Houser [9] demonstrate the powerful influence of tooth friction on the vibro-acoustic performance of gears.

Due to the involute shape of gear teeth, the mesh contact undergoes rolling and sliding, resulting in sliding friction force normal to the line of action. Variable friction coefficients are applied in studies of gear wear and power efficiency. The coefficient of friction is a function of sliding velocity, surface roughness, lubrication film,

*Corresponding author. Tel.: +1 614 688 3922.
E-mail address: parker.242@osu.edu (R.G. Parker).

0022-460X/$ - see front matter © 2008 Elsevier Ltd. All rights reserved.
doi:10.1016/j.jsv.2008.08.021

contact load, temperature, etc. Theoretical friction coefficients are derived from elasto-hydrodynamic lubrication and tribology theory [10–12]. The experimental works in Refs. [6,9,13], however, show that a constant friction coefficient is acceptable for dynamic analysis. The measured dynamic friction loads show friction coefficients of approximately 0.04–0.06 [13]. Benedict and Kelley's empirical equation shows the coefficient of friction varies between 0.03 and 0.1 [14]. The value of 0.1 (not typical condition of well-lubricated gears) is commonly used in gear dynamics [6,15–18].

The effects of tooth friction include moments about the gear centers from friction forces perpendicular to the line of action (affecting gear rotations), excitation of off-line-of-action gear translations, nonlinear dependence of friction on the sliding velocity, and energy dissipation. Iida et al. [19] examine time-varying tooth friction using a simplified dynamic model with friction as excitation and damping. Hochmann [20] focuses on the periodic external excitation from tooth friction while assuming constant mesh stiffness. Gunda and Singh [18] and Vaishya and Singh [16,17] present dynamic rotational models. The sliding mechanism is formulated based on dynamic mesh force, and the friction term appears with time-varying parameters. Parametric excitation also results from variable mesh stiffness that causes instability and severe vibrations at certain mesh frequencies [5,21–25]. Vaishya and Singh [16] apply Floquet theory to their dynamic rotational model to study parametric instabilities from variable mesh stiffness and tooth friction.

Previous works focus on models having only rotational degrees of freedom, where the only contributions from tooth friction are moments about the gear centers. Translational–rotational models are studied recently [26]. Friction force, however, also affects gear tooth bending [27], which has not been previously examined for gear dynamics. This paper develops and analyzes a dynamic translational–rotational model admitting this additional contribution of tooth friction (bending effect) as well as gear translations. The model includes this friction bending effect combined with time-varying friction force orthogonal to the line of action, time-varying mesh stiffness, and contact loss nonlinearity. The friction bending effect is shown to be important for instability and dynamic response of gear mesh deflections. Parametric instabilities and quasi-periodic response due to friction and modal interactions are studied. An iterative numerical method based on Floquet–Liapunov theory and Peano–Baker series is proposed for stability analysis. This method is evaluated against a well-known numerical method. Furthermore, perturbation analysis is conducted to find approximate solutions that predict and explain the numerical parametric instabilities. The predicted instabilities occur in practical gears as resonance-like vibration near the mesh frequency and particular multiples of mesh frequency that are close to natural frequencies in combination. The large response triggers tooth separation nonlinearity that bounds the vibration. The effects of time-varying friction moment and friction bending effect are found to be critical for combination instabilities and certain single-mode instabilities. The impacts of friction coefficient, bending effect, contact ratio, and modal damping on stability boundaries are revealed. Finally, the bending effect of tooth friction on nonlinear dynamic response is discussed and validated by finite element results.

2. Tooth bending effect of friction force

The elastic deflection of a pair of loaded gear teeth consists of deflection of the tooth as a cantilever beam, gear body flexibility, and Hertzian contact compression. The normal contact force and tangential friction force both contribute to tooth bending. Tooth bending deflection for mesh force along the line of action is studied as a non-uniform cantilever beam in Ref. [27]. Extending that derivation to include friction perpendicular to the line of action gives the total deflection of a pair of loaded gear teeth as

$$W = \left(\frac{g_c \cos\varphi_c - g_s \sin\varphi_c}{\mathrm{EI}} + \frac{1}{k_r}\right) N_{1,i} + \left(\frac{g_c \sin\varphi_c - g_s \cos\varphi_c}{\mathrm{EI}} + \frac{1}{k_r}\right) f_{1,i}, \tag{1}$$

where $N_{1,i}$ and $f_{1,i}$ are contact and friction forces of tooth pair i, respectively; φ_c is the pressure angle at the current mesh position; EI denotes tooth bending rigidity; g_c and g_s are tooth geometric factors based on parameters defined in Ref. [27]; and k_r is the effective rotational stiffness of the gear flank as reduced from Lee et al. [27], which is assumed the same for both forces. Although the compliance for $N_{1,i}$ is softer than that for $f_{1,i}$, they are of the same order.

To demonstrate the significance of the friction bending effect, a pilot study static analysis is conducted on a pair of spur gears in Fig. 1a. Gear 1 is loaded with torque T_1 and gear 2 is fixed. The equilibrium conditions

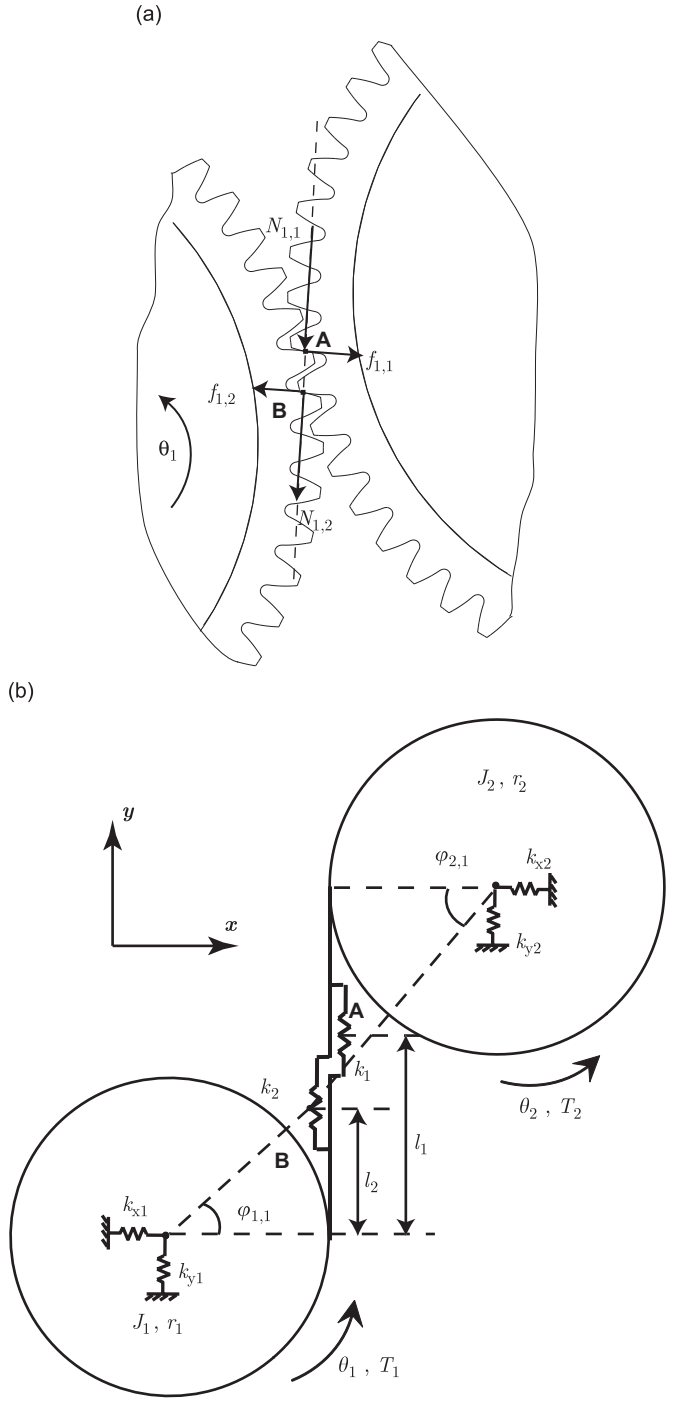

Fig. 1. (a) Mesh forces A and B are contact positions of the two tooth pairs. (b) Dynamic model of two gears with tooth friction.

yield the resultant contact and friction forces

$$N_1 = \sum_{i=1}^{z} N_{1,i} = \frac{T_1}{r_1 - \sum_{i=1}^{z} \mathrm{sgn}(v_i)\mu_i l_i \alpha_i}, \quad f_1 = \sum_{i=1}^{z} f_{1,i} = -N_1 \sum_{i=1}^{z} \mathrm{sgn}(v_i)\mu_i \alpha_i, \tag{2}$$

where $r_{1,2}$ denotes gear base radii; z is the number of tooth pairs in contact; v_i, μ_i and l_i are sliding velocities, friction coefficients and friction force moment arms (Fig. 1b), respectively; and $\alpha_i = N_{1,i}/N_1$ are load sharing factors between the z tooth pairs. The contact force of tooth pair i is $\alpha_i N_1$ and the friction force is $\mu_i \alpha_i N_1$ according to Coulomb friction.

The friction moments about the gear centers depend on the position of the contact points. The moment arms of friction forces $f_{1,i}$ in Fig. 1a are shown in Fig. 2a. The difference between the two moment arms is a base pitch and $\rho_0 = r_1 \tan\varphi$, $\rho_1 = \rho_0 - 2\pi\gamma r_1$, and $\rho_2 = \rho_0 + 2\pi(c-1)r_1$, where φ is the pressure angle at the pitch point and c is the contact ratio. γ denotes the position in a mesh period where double-tooth contact starts.

Contact force variations results from the friction force. These variations *relative to the frictionless condition* are

$$\Delta N_1 = N_1 - \frac{T_1}{r_1} = N_1 \sum_{i=1}^{z} \mathrm{sgn}(v_i)\mu_i \alpha_i l_i / r_1, \quad \Delta f_1 = -N_1 \sum_{i=1}^{z} \mathrm{sgn}(v_i)\mu_i \alpha_i, \tag{3}$$

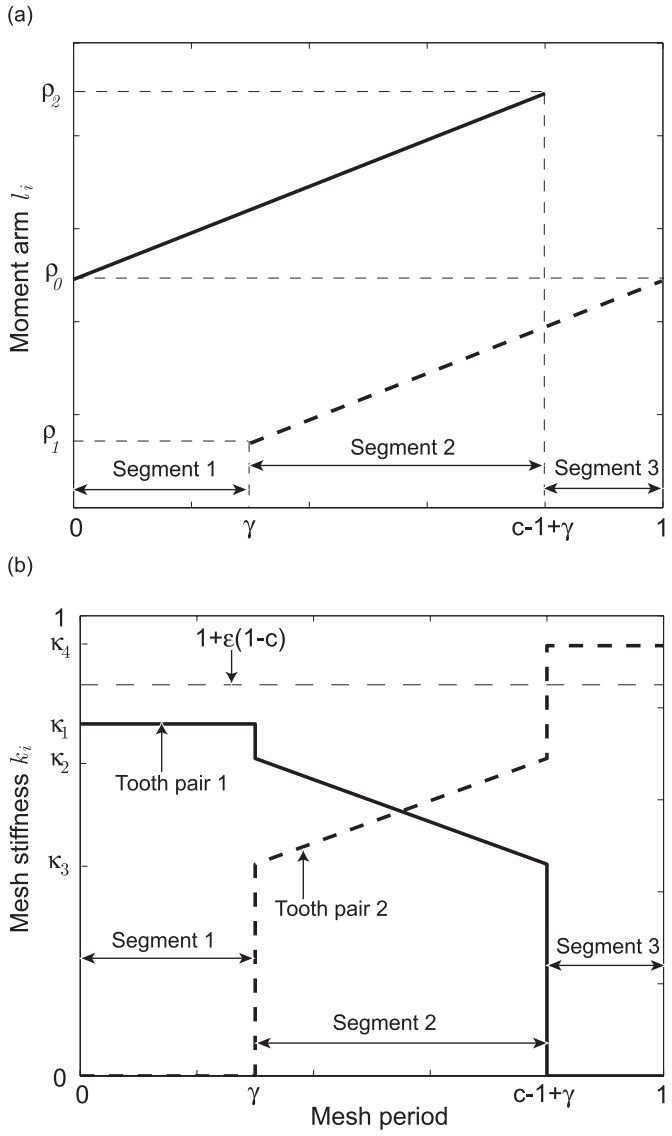

Fig. 2. (a) Moment arms of two friction forces. (b) Mesh stiffnesses (normalized by $\bar{k}$) of gear tooth pairs including friction bending effect (—— the first tooth pair; -- the second tooth pair).

where N_1 is greater than the nominal contact force T_1/r_1 when contact occurs in the approach region ($\mathrm{sgn}(v_i)=1$) where the sliding makes gear 1 approach gear 2. On the other hand, N_1 is smaller than the nominal force when contact occurs in the recess region ($\mathrm{sgn}(v_i)=-1$) where the sliding acts to separate gear 1 from gear 2. In practice, $l_i/r_1<1$ implying $|\Delta N_1|<|\Delta f_1|$. From Eqs. (1) and (3), mesh deflection variation due to tooth friction is $\Delta W=\Delta N_1/k_m+\Delta f_1/k_{\mathrm{fb}}$, where k_m and k_{fb} are the mesh stiffness and friction bending stiffness, respectively, which are reciprocals of the compliances in Eq. (1). ΔW includes the impact of friction moments and the bending effect of friction forces. Note that the traditional analytical mesh deflection variation is $\Delta W=\Delta N_1/k_m$, which only considers the moments of friction forces.

A specialized finite element program is used to benchmark the analytical model. The finite element model uses detailed contact analysis including Coulomb friction and careful tracking of the tooth contact kinematics. Its main features and validation against nonlinear gear vibration experiments are outlined in Refs. [28,29].

Variations of mesh deflection of the gear pair in Table 1 and $\mu_1=\mu_2=\mu=0.1$, obtained by finite element and analytical predictions are shown in Fig. 3. Significant differences emerge from the friction bending effect. For a contact ratio less than two, there is a pair of gear teeth engaged from mesh period 0 (pitch point) to 0.84. Another gear pair starts contact from 0.1 to 1. For single-tooth contact in the recess region (mesh period $\in(0,0.1]$), $\Delta N_1=-\mu_1 l_1 N_1/r_1<0$ such that $\Delta W\approx-2\,\mu\mathrm{m}$ when the friction bending effect is neglected. The bending effect of friction force $\Delta f_1=\mu_1 N_1>0$, however, increases the mesh deflection by about $0.5\,\mu\mathrm{m}$. Combining the effects of friction force moment and bending, $\Delta W\approx-1.5\,\mu\mathrm{m}$. The mesh deflection variation from the friction bending effect is 25% of the variation from the friction moment alone. For single-tooth

Table 1
Parameters of example gears

	Pinion	Gear
Number of teeth	38	55
Modulus (mm)	2.54	2.54
Base radius (mm)	45.35	65.64
Inertias I_i ($\mathrm{kg\,m^2}$)	2.62e−3	3.27e−3
Mesh parameters	$\bar{k}=2.98\mathrm{e}8\,\mathrm{N/m}$, $T_1=100\,\mathrm{Nm}$, $c=1.4$ $\alpha=0.6$, $\gamma=0.28$	

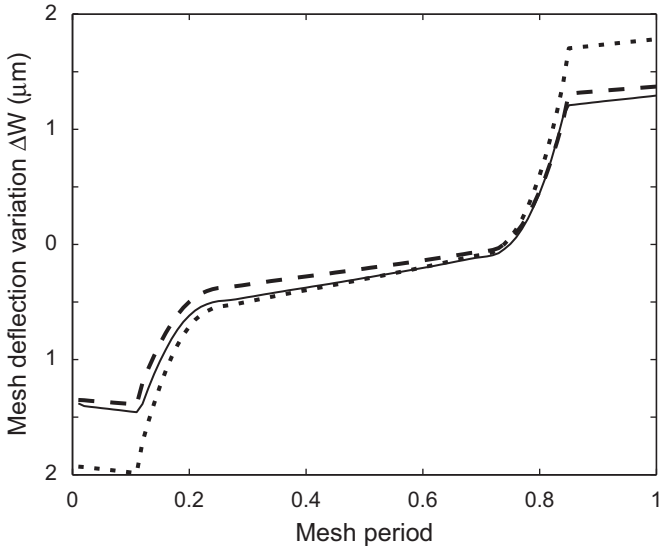

Fig. 3. Mesh deflection variation comparisons for gears in Table 1 and $T_1=100\,\mathrm{N\,m}$ (—: finite element $\mu=0.1$; - - : analytical result with friction bending and $\mu=0.1$; …: analytical result without friction bending and $\mu=0.1$).

contact in the approach region (mesh period $\in(0.84, 1]$), $\Delta N_1 = \mu_2 l_2/r_1 N_1 > 0$ such that, without the friction bending effect, $\Delta W \approx 1.75\,\mu m$, which has smaller magnitude than in the recess region due to $l_1 > l_2$ (Fig. 2a). The bending effect of friction force $\Delta f_1 = -\mu_2 N_1 < 0$ decreases the mesh deflection by about $0.5\,\mu m$, similar to the recess region because $|\Delta f_1|$ is the same for the recess and approach regions. Combining the effects of friction force moment and bending, $\Delta W \approx 1.25\,\mu m$. The mesh deflection variation from the friction bending effect is 28% of the variation from friction moment. Thus, the effect of friction force moment and bending are significant for mesh defection in the single-tooth contact region. Note that pure rolling occurs at the pitch point (mesh period = 0) such that $\Delta N_1 = \Delta f_1 = 0$ and $\Delta W = 0$. The mesh deflection and friction force are discontinuous at the pitch point due to the discontinuity of sliding velocity direction. For the double-tooth region (mesh period $\in(0.1, 0.84]$), $\Delta N_1 = (\mu_2\alpha_2 l_2 - \mu_1\alpha_1 l_1)/r_1 N_1 \approx 0$ and $\Delta W \approx 0$. In addition, $\Delta f_1 = (\mu_1\alpha_1 - \mu_2\alpha_2)N_1 \approx 0$ due to the cancellation from two tooth pairs. Thus, the effect of friction force is negligible in this area. This may not be the case in dynamic analysis, however.

Summarizing, the contribution of tooth bending caused by friction to static mesh deflection is comparable to that from the friction force moment. The static analysis example shows that friction moments lower the static transmission error in the recess region of single-tooth contact and increase the static transmission error in the approach region of single-tooth contact. The friction bending effect, however, counteracts static transmission error variations arising from the friction moment in the static case. Thus, the combined effect of friction moment and friction bending on static transmission error variation (relative to the frictionless case) is destructive and so the individual effects are less evident in measured static transmission error. As will be shown, the combined effect in the dynamic case is more complex, however, and can be destructive or constructive depending on the modal properties. The interaction between this friction bending effect and other time-varying parameters is potentially important to the stability and dynamic response.

3. Mathematical model

3.1. Modeling of friction bending effect

For involute gear teeth, variation of mesh stiffness and tooth friction are the only excitations in this work. In contrast to existing gear models that treat gear meshes as one elastic element even when multiple tooth pairs are in contact, this study models each tooth pair as a separate elastic element, and they are connected in parallel. Although the number of tooth pairs in contact varies as the gears roll, by assigning zero mesh stiffness for the tooth pair out of contact there are always $Z = \text{ceil}(c)$ pairs of teeth in contact during a mesh period, where c is the contact ratio and ceil(c) gives the smallest integer greater than c.

Mesh stiffness usually reflects the linear relation between normal load and mesh deflection. As discussed above, however, the bending effect of friction forces gives rise to pronounced impact on mesh deflection. In other words, applying the same normal load, the mesh deflections are different for friction and frictionless conditions. This contribution from friction bending can be included in an effective mesh stiffness. Substituting Eq. (2) into Eq. (1) and isolating $W/N_{1,i}$, the mesh stiffness of tooth pair i including the effect of friction bending is

$$k_i = \frac{N_{1,i}}{W} = \tilde{k}_i[1 - \text{sgn}(v_i)\tilde{\beta}\mu_i]^{-1} \approx \tilde{k}_i[1 + \text{sgn}(v_i)\tilde{\beta}\mu_i],$$
$$\tilde{\beta} = \frac{g_c \sin\varphi_c - g_s \cos\varphi_c + \text{EI}/k_r}{g_c \cos\varphi_c - g_s \sin\varphi_c + \text{EI}/k_r}, \quad |\text{sgn}(v_i)\tilde{\beta}\mu_i| \ll 1, \tag{4}$$

where $\tilde{\beta}$ is the ratio of compliances of the two forces in Eq. (1), $\tilde{k}_i$ is the mesh stiffness without friction, and k_i is the effective mesh stiffness with friction. $\tilde{\beta}$ is less than 1 and varies periodically over a mesh cycle. The mean value of $\tilde{\beta}$ is used in this study.

From Eq. (4), the effective mesh stiffness is affected by the compliance ratio, friction coefficient and dynamic sliding velocity from nominal gear speed and gear vibration. The effect of the vibratory velocity, however, is negligible compared to the nominal velocity $\bar{v}_i = \Omega_1 r_1(\tan\varphi_{1,i} - \tan\varphi_{2,i})$, where Ω_1 is the nominal rotation speed of the input gear and $\varphi_{z,i}$ is the pressure angle of tooth i of gear z [16,17]. Low contact ratio gears ($c < 2$) are considered in this study such that $Z = 2$. For the mesh cycle shown in Fig. 2, the pitch point is at zero, and the tooth pair in contact from mesh period 0 to $c - 1 + \gamma$, defined as the first tooth pair, is in the

recess region ($\mathrm{sgn}(v_1)<0$). The second tooth pair engages from γ to 1 and it is in the approach region ($\mathrm{sgn}(v_2)>0$).

Defining $\bar{k}$ as the mean value of frictionless mesh stiffness and ε as the ratio of peak–peak to mean value of the mesh stiffness, the *frictionless* mesh stiffnesses are $\tilde{k}_1=\bar{k}[1+\varepsilon(1-c)]$ and $\tilde{k}_2=0$ for segment 1 (indicated in Fig. 2b), and $\tilde{k}_1=0$, $\tilde{k}_2=\bar{k}[1+\varepsilon(1-c)]$ for segment 3. In segment 2, two tooth pairs share the gear load such that $\tilde{k}_1$ decreases linearly from $\alpha\bar{k}[1+\varepsilon(2-c)]$ to $(1-\alpha)\bar{k}[1+\varepsilon(2-c)]$ and $\tilde{k}_2$ increases from $(1-\alpha)\ \bar{k}[1+\varepsilon(2-c)]$ to $\alpha\bar{k}[1+\varepsilon(2-c)]$, where α is the load sharing factor at mesh period γ. α is approximated by the ratio of the static load of tooth pair 1 to the resultant tooth load, which is calculated by finite element analysis. Note that $\tilde{k}_1+\tilde{k}_2=\bar{k}[1+\varepsilon(1-c)]$ for single-tooth contact and $\tilde{k}_1+\tilde{k}_2=\bar{k}[1+\varepsilon(2-c)]$ for double-tooth contact.

The quasi-static *frictional* mesh stiffnesses shown in Fig. 2b are found by substituting the above $\tilde{k}_i$ into Eq. (4). The mesh stiffnesses normalized by $\bar{k}$ are

$$\begin{aligned}
&\text{Segment 1}: k_1/\bar{k}=\kappa_1=(1-\beta)[1+\varepsilon(1-c)], \quad k_2=0\\
&\text{Segment 2}: k_1/\bar{k} \text{ varies linearly from } \kappa_2 \text{ to } \kappa_3, k_2/\bar{k} \text{ varies linearly from } \kappa_3 \text{ to } \kappa_2\\
&\kappa_2=\alpha(1-\beta)[1+\varepsilon(2-c)], \quad \kappa_3=(1-\alpha)(1+\beta)[1+\varepsilon(2-c)]\\
&\text{Segment 3}: k_1=0, \quad k_2/\bar{k}=\kappa_4=(1+\beta)[1+\varepsilon(1-c)],
\end{aligned} \tag{5}$$

where $\beta=\tilde{\beta}\mu$ is the friction bending factor. The frictional mesh stiffnesses in segments 1 and 3 are reduced and increased by β, respectively, due to the friction bending effect. The mesh stiffnesses of high contact ratio gears ($c>2$) can be treated in a similar way.

3.2. Dynamic model of gear pair with tooth friction

Referring to Fig. 1a, the dynamic normal forces $N_{z,i}$ and friction forces $f_{z,i}$ act at the mesh positions A and B. Elasticity of each tooth pair is captured by the variable mesh stiffnesses $k_{1,2}$ in Fig. 1b. To visually emphasize the parallel connection of stiffnesses for the individual tooth pairs, each elastic mesh element is artificially shifted slightly in the x direction. The normal forces and mesh stiffnesses, however, are actually collinear along the line of action. The gear translations are constrained by bearings with lateral stiffnesses k_{xz} and k_{yz}. $J_{1,2}$ are polar moments of inertia. $\theta_{1,2}$ are vibratory gear rotations. T_1 and T_2 are the input torque and load, respectively. Dynamic transmission error $u=r_1\theta_1+r_2\theta_2$ is introduced to remove the rigid body mode.

The equations of motion can be derived by Newtonian or Lagrangian methods to obtain

$$J_1\ddot{\theta}_1=-k_m(u+y_1-y_2)r_1-\mu\sum_{i=1}^{Z}\mathrm{sgn}(v_i)\Gamma_i k_i(u+y_1-y_2)l_i+T_1, \tag{6}$$

$$J_2\ddot{\theta}_2=-k_m(u+y_1-y_2)r_2-\mu\sum_{i=1}^{Z}\mathrm{sgn}(v_i)\Gamma_i k_i(u+y_1-y_2)(D-l_i)+T_2, \tag{7}$$

$$m_1\ddot{x}_1=-k_{x1}x_1-\mu\sum_{i=1}^{Z}\mathrm{sgn}(v_i)\Gamma_i k_i x_1, \tag{8}$$

$$m_1\ddot{y}_1=-k_{y1}y_1-k_m(u+y_1-y_2), \tag{9}$$

$$m_2\ddot{x}_2=-k_{x2}x_2-\mu\sum_{i=1}^{Z}\mathrm{sgn}(v_i)\Gamma_i k_i x_2, \tag{10}$$

$$m_2\ddot{y}_2=-k_{y2}y_2-k_m(u+y_1-y_2). \tag{11}$$

Multiplying Eq. (1) with r_1/J_1 and Eq. (2) with r_2/J_2 and summing them yields

$$J_e\ddot{u}+\left\{\mu\sum_{i=1}^{Z}[\eta l_i/r_1+(1-\eta)(D-l_i)/r_2]\mathrm{sgn}(v_i)\Gamma_i k_i+k_m\right\}(u+y_1-y_2)=\frac{T_1}{r_1}. \tag{12}$$

Combining Eqs. (8)–(11) and (12), the equations of motion in matrix form are

$$
\begin{aligned}
&\mathbf{M}\ddot{\mathbf{x}} + \mathbf{C}\dot{\mathbf{x}} + [\mathbf{L}(\mathbf{x}) + \mathbf{K}(\mathbf{x})]\mathbf{x} = \mathbf{F},\\
&\mathbf{M} = \mathrm{diag}([J_e, m_1, m_1, m_2, m_2]), \quad J_e = J_1 J_2/(r_2^2 J_1 + r_1^2 J_2),\\
&\mathbf{X} = [u, x_1, y_1, x_2, y_2]^{\mathrm{T}}, \quad \mathbf{F} = [T_1/r_1, 0, 0, 0, 0]^{\mathrm{T}},\\
&\mathbf{L} = \begin{bmatrix} L_m & 0 & L_m & 0 & -L_m \\ -L_\mu & 0 & -L_\mu & 0 & L_\mu \\ 0 & 0 & 0 & 0 & 0 \\ L_\mu & 0 & L_\mu & 0 & -L_\mu \\ 0 & 0 & 0 & 0 & 0 \end{bmatrix}, \quad \mathbf{K} = \begin{bmatrix} k_m & 0 & k_m & 0 & -k_m \\ 0 & k_{x1} & 0 & 0 & 0 \\ k_m & 0 & k_m + k_{y1} & 0 & -k_m \\ 0 & 0 & 0 & k_{x2} & 0 \\ -k_m & 0 & -k_m & 0 & k_m + k_{y2} \end{bmatrix},\\
&L_m = \mu \sum_{i=1}^{Z} [\eta l_i/r_1 + (1-\eta)(D - l_i)/r_2]\mathrm{sgn}(v_i)\Gamma_i k_i,\\
&L_\mu = \mu \sum_{i=1}^{Z} \mathrm{sgn}(v_i)\Gamma_i k_i,\\
&v_i \approx \bar{v}_i = \Omega_1 r_1(\tan\varphi_{1,i} - \tan\varphi_{2,i}),\\
&\Gamma_i = \tfrac{1}{2}[\mathrm{sgn}(u + y_1 - y_2 - g_i) + \mathrm{sgn}(u + y_1 - y_2 - g_i + B)],\\
&k_m = \sum_{i=1}^{Z} \Gamma_i k_i,
\end{aligned}
\tag{13}
$$

where L_m and L_μ include the contributions of tooth friction on rotations and off-line-of-action translations, respectively; $\eta = r_1^2 J_2/(r_2^2 J_1 + r_1^2 J_2)$; $l_i = r_1 \tan\varphi_{1,i}$ are moment arms of the friction force $f_{1,i}$ with respect to the center of gear 1; $D = (r_1 + r_2)\tan\varphi$ is the length of the line of action; B is the gear backlash; the tooth separation function $\Gamma_i \in \{1, 0, -1\}$ determines the existence of drive-side contact $(+1)$, contact loss (0) or backside contact (-1); and g_i is the tooth surface deviation, which is taken as zero in this study. The constant matrix $\mathbf{C}$ is determined from a modal damping ratio ζ whose fluctuation has no significant impact on parametric excitation [30]. In L_m, the time-varying mesh stiffness and friction bending effect are included through k_i, and the time-varying moment arm of the friction force is included through l_i. These are all parametric excitations. L_μ only includes parametric excitations from mesh stiffness variation and friction bending effect. $\mathrm{sgn}(v_i)$ and Γ_i are the nonlinearities.

The power from the friction force is always negative for motion in any of the degrees of freedom because the friction force always opposes the direction of sliding velocity. As a result, friction dissipates energy, as expected. In addition, however, the friction force, moment of friction force, and friction bending effect are time-varying, periodic parametric excitations that excite the system and can, under resonant conditions as analyzed subsequently, pump energy into the system and lead to large vibration.

The governing equation (13) is a group of nonlinear, time-varying differential equations. Parametric excitations are included in $\mathbf{L}$ and $\mathbf{K}$ from the time-varying friction moment arms l_i and mesh stiffnesses k_i modified by the friction bending effect.

Substitution of $\bar{k}$ for k_m in $\mathbf{K}$ yields $\bar{\mathbf{K}}$. The eigenvalue problem for the linear time-invariant form of Eq. (13) averaged over a mesh cycle is $\bar{\mathbf{K}}\phi_n = \omega_n^2 \mathbf{M}\phi_n$ where $f_n = \omega_n/(2\pi)$ are natural frequencies. The normalized vibration modes are

$$
\begin{aligned}
\phi_n &= [\phi_{n1}, 0, \phi_{n3}, 0, \phi_{n5}]^{\mathrm{T}}, \quad n = 1, 2, 3,\\
\phi_4 &= [0, \phi_{n2}, 0, 0, 0]^{\mathrm{T}}, \quad \phi_5 = [0, 0, 0, \phi_{n4}, 0]^{\mathrm{T}},
\end{aligned}
\tag{14}
$$

where ϕ_{nr} are elements of the nth vibration mode. Rotational modes ($n = 1,2,3$) have coupled motions of u, y_1 and y_2. Translational modes ($n = 4,5$) only have off-line-of-action translations x_1 and x_2.

To examine the parametric instabilities, we take $\Gamma_i = 1$ (contact loss occurs only after onset of large vibration). Eq. (13) becomes a linear, time-varying model with periodic, piecewise linear parametric excitations in a mesh period T. The mesh stiffnesses and moment arms vary in each of three segments in a period (Fig. 2). Combining Eqs. (5) and (13), the time-varying elements of $\mathbf{L}$ and $\mathbf{K}$ are as follows.

For segment 1 ($t_0 \leqslant t < t_1$ where $t_0 = 0$ and $t_1 = \gamma T$)

$$\begin{array}{lcl} k_1 = \kappa_1 \bar{k} & & k_m = (1-\beta)[1+\varepsilon(1-c)]\bar{k}, \\ k_2 = 0 & \Rightarrow & L_\mu = \mu(1-\beta)[1+\varepsilon(1-c)]\bar{k}, \\ l_1 = \rho_0 + r_1 \Omega t & & L_m = L_{1,0} + L_{1,1} t. \end{array} \tag{15}$$

For segment 2 ($t_1 \leqslant t < t_2$ where $t_2 = (c+\gamma-1)T$)

$$\begin{array}{lcl} k_1 = \kappa_2 \bar{k} - (t-t_1)w & & k_m = (\kappa_2+\kappa_3)\bar{k}, \\ k_2 = \kappa_3 \bar{k} + (t-t_1)w & \Rightarrow & L_\mu = \mu\bar{k}(\kappa_3-\kappa_2) + 2(t-t_1)\mu w, \\ l_1 = \rho_1 + (t-t_1) r_1 \Omega & & L_m = L_{2,0} + (t-t_1)L_{2,1} + (t-t_1)^2 L_{2,2}. \end{array} \tag{16}$$

For segment 3 ($t_2 \leqslant t < t_3$ where $t_3 = T$)

$$\begin{array}{lcl} k_1 = 0 & & k_m = (1+\beta)[1+\varepsilon(1-c)]\bar{k} \\ k_2 = \kappa_4 \bar{k} & \Rightarrow & L_\mu = \mu(1+\beta)[1+\varepsilon(1-c)]\bar{k} \\ l_1 = \rho_2 + (t-t_2) r_1 \Omega & & L_m = L_{3,0} + (t-t_2)L_{3,1}. \end{array} \tag{17}$$

where $w = (\kappa_2 - \kappa_3)/(t_3 - t_2)$, Ω is the mesh frequency, $L_{p+1,q}$ (segment index $p = 0,1,2$) are coefficients that emerge from simplification of L_m (see Appendix A), and $\rho_{0,1,2}$ are defined previously in Fig. 2b.

Substitution of Eqs. (15)–(17) into Eq. (13) yields different matrices $\mathbf{L}$ and $\mathbf{K}$ for each segment. These matrices, however, have the common form

$$\begin{aligned} \mathbf{L} &= \mathbf{L}_a + (t-t_p)\mathbf{L}_b + (t-t_p)^2 \mathbf{L}_c, \\ \mathbf{K} &= \mathbf{K}_a + (t-t_p)\mathbf{K}_b + (t-t_p)^2 \mathbf{K}_c \quad \text{for } 0 \leqslant t < T, \end{aligned} \tag{18}$$

where $\mathbf{L}_{a,b,c}$ result from substitution of $L_{p+1,q}$ and L_μ into $\mathbf{L}$. $\mathbf{K}_{a,b,c}$ result from substitution of k_m into $\mathbf{K}$. $\mathbf{L}_{a,b,c}$ and $\mathbf{K}_{a,b,c}$ are different for each segment due to variations of mesh stiffnesses and moment arms. For the rectangular shape mesh stiffnesses used in this work, $\mathbf{K}_{b,c} = 0$ for all segments, but that is not true for general stiffness variations. Note $\mathbf{L}$ and $\mathbf{K}$ are periodic operators with period T.

With substitution of Eq. (18), Eq. (13) is recast into homogeneous state-space form as

$$\begin{aligned} &\dot{\mathbf{y}} = \mathbf{G}(t)\mathbf{y} \quad \text{for } 0 \leqslant t < T, \\ &\mathbf{y} = [\mathbf{x}, \dot{\mathbf{x}}]^{\mathrm{T}}, \quad \mathbf{G} = \begin{pmatrix} \mathbf{0} & \mathbf{I} \\ -\mathbf{M}^{-1}(\mathbf{K}+\mathbf{L}) & -\mathbf{M}^{-1}\mathbf{C} \end{pmatrix} = \mathbf{G}_a + (t-t_p)\mathbf{G}_b + (t-t_p)^2 \mathbf{G}_c, \end{aligned} \tag{19}$$

where $\mathbf{G}(t+T) = \mathbf{G}(t)$.

4. Parametric instability

4.1. Calculation of the state transition matrix

According to Floquet–Liapunov theory [31], the fundamental matrix $\mathbf{\Pi}(t)$ comprised of a complete set of fundamental solutions for Eq. (19) satisfies $\mathbf{\Pi}(t) = \mathbf{P}(t)\mathrm{e}^{(t-t_0)\mathbf{Q}}$, where $\mathbf{P}(t)$ is a periodic function with period T, $\mathbf{Q}$ is a complex constant matrix, and t_0 is the initial time. After one period T,

$$\mathbf{\Pi}(t+T) = \mathbf{P}(t+T)\mathrm{e}^{(t+T-t_0)\mathbf{Q}} = \mathbf{\Pi}(t)\mathrm{e}^{\mathbf{Q}T}, \tag{20}$$

where $e^{\mathbf{Q}T} = \mathbf{\Pi}^{-1}(t_0)\mathbf{\Pi}(t_0+T) = \mathbf{\Phi}(t_0+T,t_0)$ is the state transition matrix or monodromy matrix. The stability of fundamental solutions is determined by the eigenvalues λ_i of the state transition matrix: $|\lambda_i|<1$ indicates stable solutions; $|\lambda_i|>1$ indicates unstable; and $\lambda_i = 1^{1/m}$ for integer m means period-mT solutions.

As discussed above, the linear, time-varying model is expressed as three polynomial matrix forms associated with the three segments of one period defined previously. The state transition matrix of the system is obtained by the state transition matrices of the three segments

$$\mathbf{\Phi}(T,0) = \mathbf{\Phi}(t_1,0)\mathbf{\Phi}(t_2,t_1)\mathbf{\Phi}(T,t_2), \tag{21}$$

where $\mathbf{\Phi}(t_{p+1},t_p) = \mathbf{\Pi}^{-1}(t_p)\mathbf{\Pi}(t_{p+1})$. The state transition matrix for any segment with $t_p \leqslant t < t_{p+1}$ is expanded using Peano–Baker series [32,33] as

$$\begin{aligned}\mathbf{\Phi}(t_{p+1},t_p) = \mathbf{I} &+ \int_{t_p}^{t_{p+1}} \mathbf{G}(\tau_0 - t_p)\mathrm{d}\tau_0 + \int_{t_p}^{t_{p+1}} \mathbf{G}(\tau_1 - t_p)\int_{t_p}^{\tau_1} \mathbf{G}(\tau_2 - t_p)\mathrm{d}\tau_2\,\mathrm{d}\tau_1 \\ &+ \int_{t_p}^{t_{p+1}} \mathbf{G}(\tau_1 - t_p)\int_{t_p}^{\tau_1} \mathbf{G}(\tau_2 - t_p)\int_{t_p}^{\tau_2} \mathbf{G}(\tau_3 - t_p)\mathrm{d}\tau_3\,\mathrm{d}\tau_2\,\mathrm{d}\tau_1 + \cdots.\end{aligned} \tag{22}$$

Let $\tilde{\tau}_i = \tau_i - t_p$ such that,

$$\int_{t_p}^{t_{i-1}} \mathbf{G}(\tau_i - t_p)\mathrm{d}\tau_i = \int_0^{t_{i-1}-t_p} \mathbf{G}(\tilde{\tau}_i)\mathrm{d}\tilde{\tau}_i \Rightarrow \mathbf{\Phi}(t_{p+1},t_p) = \mathbf{\Phi}(h_p,0), \tag{23}$$

where $h_p = t_{p+1} - t_p$. Evaluation of the integrals in Eq. (22) and the polynomial form of $\mathbf{G}$ gives a recursive sequence for calculation of the state transition matrix as

$$\begin{aligned}&\mathbf{\Phi}_P(h_p,0) = \mathbf{I} + \mathbf{T}_1(h_p) + \mathbf{T}_2(h_p) + \cdots + \mathbf{T}_n(h_p) + \cdots, \\ &\mathbf{T}_1 = \sum_{i=1}^{3} \mathbf{T}_{1,i} = \mathbf{G}_0 h_p + \mathbf{G}_1 h_p^2/2 + \mathbf{G}_2 h_p^3/3, \\ &\mathbf{T}_n = \sum_{i=1}^{2n+1} \mathbf{T}_{n,i} \quad n \geqslant 2, \\ &\mathbf{T}_{n,1} = \frac{1}{n} h_p \mathbf{G}_0 \mathbf{T}_{n-1,1}, \\ &\mathbf{T}_{n,2} = \frac{h_p}{n+1}(\mathbf{G}_0 \mathbf{T}_{n-1,2} + h_p \mathbf{G}_1 \mathbf{T}_{n-1,1}), \\ &\mathbf{T}_{n,i} = \frac{1}{n+i-1}\sum_{j=0}^{2} h_p^{j+1} \mathbf{G}_j \mathbf{T}_{n-1,i-j}, \quad i = 3,4,\ldots 2n-1, \\ &\mathbf{T}_{n,2n} = \frac{h_p^2}{3n-1}(\mathbf{G}_1 \mathbf{T}_{n-1,2n-1} + h_p \mathbf{G}_2 \mathbf{T}_{n-1,2n-2}), \\ &\mathbf{T}_{n,2n+1} = \frac{1}{3n} h_p^3 \mathbf{G}_2 \mathbf{T}_{n-1,2n-1},\end{aligned} \tag{24}$$

where $\mathbf{T}_n$ denotes the sequence of terms in Eq. (22).

For comparison, a numerical integration method [34–36] is applied. The time span h_p is discretized into m divisions, where Δ_i is the time step of division i ($t_i < t \leqslant t_{i+1}$) and $\mathbf{C}_i$ is the mean value of $\mathbf{G}$ over a mesh cycle. Thus,

$$\begin{aligned}&\mathbf{\Phi}_I(h_p,0) = \prod_{i=1}^{m}[I + \Delta_i \mathbf{C}_i + \tfrac{1}{2}(\Delta_i \mathbf{C}_i)^2 + \cdots + \tfrac{1}{k!}(\Delta_i \mathbf{C}_i)^k + \cdots] \\ &\mathbf{C}_i = \frac{1}{\Delta_i}\int_{\Delta_i} (\mathbf{G}_0 + \mathbf{G}_1\tau + \mathbf{G}_2\tau^2)\mathrm{d}\tau = \mathbf{G}_0 + \frac{t_{i+1}+t_i}{2}\mathbf{G}_1 + \frac{t_{i+1}^3 - t_i^3}{3\Delta_i}\mathbf{G}_2.\end{aligned} \tag{25}$$

The numerical integration method applies for arbitrary functions $\mathbf{G}$. The recursive process applies only to $\mathbf{G}$ having polynomial forms.

To validate the recursive process and compare performance against numerical integration, an example system is selected as

$$\ddot{x} + [a(t - nT) + b]x = 0, \quad nT \leqslant t < (n+1)T. \tag{26}$$

The stiffness term is a periodic sawtooth function. The fundamental and state transition matrices are [31]

$$\mathbf{\Pi}(t) = \begin{bmatrix} \sqrt{at+b}J_{1/3}(\sigma) & \sqrt{at+b}J_{-1/3}(\sigma) \\ (at+b)J_{-2/3}(\sigma) & -(at+b)J_{2/3}(\sigma) \end{bmatrix}, \quad \sigma = \frac{2(at+b)^{3/2}}{3a}, \tag{27}$$

$$\mathbf{\Phi}_B(h_p, 0) = \mathbf{\Pi}^{-1}(0)\mathbf{\Pi}(h_p). \tag{28}$$

The relative error of the recursive process with respect to the analytical solution is examined in Fig. 4a. There is a critical value n_c for a given h_p above which the error is insensitive to n and the error is extremely small. The errors in the integration method shown in Fig. 4b are higher than for the recursive process for

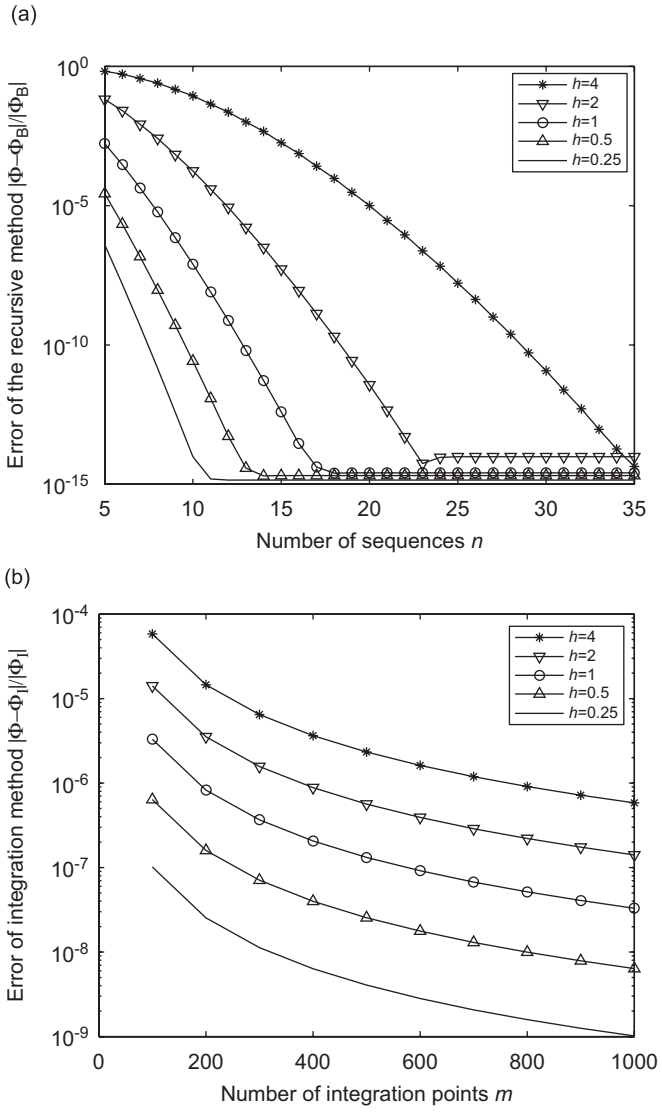

Fig. 4. (a) Comparison of Peano–Baker series solution with analytical solution. (b) Comparison of the integration method with analytical solution ($a = -1$, $b = -1$). —✳— $h = 4$, —▽— $h = 2$, —○— $h = 1$, —△— $h = 0.5$, —— $h = 0.25$.

comparable computation. Computation for the recursive process is slightly less than the integration method given $n = 20$, $m = 200$ and $h_p = 0.5$.

The recursive and numerical integration methods use Peano–Baker and exponential series expansions, respectively. Both have truncation errors. The truncation error of exponential series is smaller than Peano–Baker series for the same number of terms. The integration method, however, has additional discretization error. On the other hand, the computational demands of the recursive process increase significantly with the number of terms. In this study, the recursive process is more efficient than the integration method because a smaller number of terms provides the required accuracy. Overall, the recursive process has better accuracy and requires less computation than numerical integration for systems expanded as polynomial forms.

4.2. Perturbation approximation

This study only considers small ratios of mesh stiffness variation to mean stiffness ($\varepsilon \ll 1$), small damping ($\zeta \ll 1$) and small coefficient of friction ($\mu \ll 1$). The nonlinear, time-varying terms in Eq. (13) for gear pairs with $c<2$ are linearized in these quantities as

$$\begin{aligned} k_m &= k_1 + k_2 = \bar{k} + \varepsilon\tilde{K} \Rightarrow \tilde{K} = (k_1 + k_2 - \bar{k})/\varepsilon, \\ L_\mu &= \mu(k_2 - k_1) = \varepsilon\tilde{L}_\mu \Rightarrow \tilde{L}_\mu = g(k_2 - k_1), \\ L_m &= \varepsilon\frac{g}{r_1 r_2}\{k_2[\eta r_2 l_2 + r_1(1-\eta)(D-l_2)] - k_1[\eta r_2 l_1 + r_1(1-\eta)(D-l_1)]\} = \varepsilon\tilde{L}, \end{aligned} \tag{29}$$

where $g = \mu/\varepsilon$ denotes the ratio of friction to mesh stiffness variation. $\tilde{K}$, $\tilde{L}_\mu$, $\tilde{L}$ and g are $O(1)$. These time-varying functions are expanded in Fourier series as

$$\tilde{L} = g\sum_{s=1}^{\infty} \Lambda_s e^{is\Omega t} + \text{c.c.}, \quad \tilde{L}_\mu = g\sum_{s=1}^{\infty} \chi_s e^{is\Omega t} + \text{c.c.}, \quad \tilde{K} = \sum_{s=1}^{\infty} \Theta_s e^{is\Omega t} + \text{c.c.}, \tag{30}$$

where Λ_s, χ_s and Θ_s are known complex Fourier amplitudes. The symbol c.c. represents the complex conjugate of preceding terms.

The associated operators are $\mathbf{L} = \varepsilon\tilde{\mathbf{L}}$ and $\mathbf{K} = \bar{\mathbf{K}} + \varepsilon\tilde{\mathbf{K}}$, where $\tilde{\mathbf{L}}$ and $\tilde{\mathbf{K}}$ are obtained from substitution of L_m, L_μ and k_m into $\mathbf{L}$ and $\mathbf{K}$. Let $\phi = [\phi_n]$ be the modal matrix from Eq. (14). Applying the modal transformation $\mathbf{x} = \boldsymbol{\phi}\mathbf{u}$, Eq. (13) is recast into modal coordinates as

$$\ddot{u}_n + 2\varepsilon\varsigma\omega_n\dot{u}_n + \omega_n^2 u_n + \varepsilon\sum_{r=1}^{5}(\phi_n^{\mathrm{T}}\tilde{L}\phi_r + \phi_n^{\mathrm{T}}\tilde{K}\phi_r)u_r = 0, \quad n = 1,2,3,4,5, \tag{31}$$

where $\varsigma = \zeta/\varepsilon = O(1)$. Using Eq. (14), $\phi_n^{\mathrm{T}}\tilde{\mathbf{L}}\phi_r$ and $\phi_n^{\mathrm{T}}\tilde{\mathbf{K}}\phi_r$ are

$$\begin{aligned} \phi_n^{\mathrm{T}}\tilde{\mathbf{L}}\phi_r &= \begin{cases} 0 & \text{if } r \geqslant 4, \\ D_{nr}\tilde{L} & \text{if } n, r < 4, \\ -D_{nr}\tilde{L}_\mu & \text{if } r<4 \text{ and } n \geqslant 4, \end{cases} \\ \phi_n^{\mathrm{T}}\tilde{\mathbf{K}}\phi_r &= \begin{cases} 0 & \text{if } r \geqslant 4 \text{ or } r<4 \text{ and } n \geqslant 4, \\ E_{nr}\tilde{K} & \text{if } n, r < 4, \end{cases} \\ D_{nr} &= \phi_{n1}(\phi_{r1} + \phi_{r3} - \phi_{r5}), \\ E_{nr} &= (\phi_{n1} + \phi_{n3} - \phi_{n5})(\phi_{r1} + \phi_{r3} - \phi_{r5}), \end{aligned} \tag{32}$$

where $D_{nr} \in \mathbb{R}$ is asymmetric and $E_{nr} = E_{rn} \in \mathbb{R}$ is symmetric. E_{nr} is the product of the mesh deflections in modes n and r. D_{nr} is the product of rotational transmission error in mode n and mesh deflection in mode r.

Substitution of Eq. (32) into Eq. (31) yields

$$\ddot{u}_n + 2\varepsilon\varsigma\omega_n\dot{u}_n + \omega_n^2 u_n + \varepsilon\sum_{r=1}^{3}(D_{nr}\tilde{L} + E_{nr}\tilde{K})u_r = 0, \quad n = 1,2,3, \tag{33}$$

$$\ddot{u}_n + 2\varepsilon\varsigma\omega_n\dot{u}_n + \omega_n^2 u_n - \varepsilon\sum_{r=1}^{3} D_{nr}\tilde{L}_\mu u_r = 0, \quad n = 4,5. \tag{34}$$

Observing the upper limit of the sum in Eq. (33), the rotation modes 1, 2 and 3 are coupled together in Eq. (33) through time-varying friction moments and mesh stiffness. Strong interactions between these modes may lead to combination instabilities. These rotation modes are decoupled from the translation modes 4 and 5 in Eq. (33). The translation modes, however, are impacted by rotation modes in Eq. (34), although no coupling exists between the two translation modes.

Applying the method of multiple scales, the solutions of Eqs. (33) and (34) are expressed as

$$u_n = u_{n,0}(t,\tau) + \varepsilon u_{n,1}(t,\tau) + \cdots \quad n = 1,2,3,4,5, \tag{35}$$

where $\tau = \varepsilon t$. Substituting Eq. (35) into Eqs. (33) and (34) and separating terms with the same power in ε yields

$$\ddot{u}_{n,0} + \omega_n^2 u_{n,0} = 0, \quad n = 1,2,3,4,5, \tag{36}$$

$$\ddot{u}_{n,1} + \omega_n^2 u_{n,1} = -2\frac{\partial^2 u_{n,0}}{\partial\tau\partial t} - 2\varsigma\omega_n\frac{\partial u_{n,0}}{\partial t} - \sum_{r=1}^{3}(D_{nr}\tilde{L} + E_{nr}\tilde{K})u_{r,0}, \quad n = 1,2,3, \tag{37}$$

$$\ddot{u}_{n,1} + \omega_n^2 u_{n,1} = -2\frac{\partial^2 u_{n,0}}{\partial\tau\partial t} - 2\varsigma\omega_n\frac{\partial u_{n,0}}{\partial t} + \sum_{r=1}^{3} D_{nr}\tilde{L}_\mu u_{r,0}, \quad n = 4,5. \tag{38}$$

The general solutions of Eq. (36) are

$$u_{n,0} = A_n(\tau)e^{i\omega_n t} + \text{c.c.}, \quad n = 1,2,3,4,5. \tag{39}$$

Substituting Eqs. (30) and (39) into Eq. (37) yields

$$\begin{aligned}\ddot{u}_{n,1} + \omega_n^2 u_{n,1} = & -2i\omega_n e^{i\omega_n t}\frac{\partial A_n}{\partial\tau} - 2\varsigma\omega_n(i\omega_n)A_n e^{i\omega_n t} \\ & - \sum_{r=1}^{3}\sum_{s=1}^{\infty}(D_{nr}g\Lambda_s + E_{nr}\Theta_s)[A_r e^{i(s\Omega+\omega_r)t} + \bar{A}_r e^{i(s\Omega-\omega_r)t}] + \text{c.c.}, \quad n = 1,2,3,\end{aligned} \tag{40}$$

where an overbar means the complex conjugate.

By letting $s\Omega = \omega_p + \omega_q + \varepsilon\sigma$ (p, $q \leqslant 3$), where σ is a detuning parameter, two-mode ($p \neq q$) combination instabilities or single-mode ($p = q$) instabilities of rotation modes are examined. Elimination of secular terms leading to unbounded response in Eq. (40) requires

$$2i\omega_p\frac{\partial A_p}{\partial\tau} + 2i\varsigma\omega_p^2 A_p + (D_{pq}g\Lambda_s + E_{pq}\Theta_s)\bar{A}_q e^{i\sigma\tau} = 0, \tag{41}$$

$$2i\omega_q\frac{\partial A_q}{\partial\tau} + 2i\varsigma\omega_q^2 A_q + (D_{qp}g\Lambda_s + E_{qp}\Theta_s)\bar{A}_p e^{i\sigma\tau} = 0. \tag{42}$$

The solutions of Eqs. (41) and (42) are

$$A_p = a_p e^{\lambda\tau}, \quad A_q = a_q e^{(\bar{\lambda}+i\sigma)\tau}, \tag{43}$$

where a_p and a_q are complex constants, and λ are roots of the characteristic equation obtained from Eqs. (41) and (42) such that

$$\lambda = \frac{1}{2}\{-\varsigma(\omega_p+\omega_q) + \mathrm{i}\sigma \pm [\varsigma^2(\omega_p-\omega_q)^2 - \sigma^2 + 2\mathrm{i}\varsigma\sigma(\omega_p-\omega_q) + \Psi]^{1/2}\},$$
$$\Psi = \frac{1}{\omega_p\omega_q}(D_{pq}g\Lambda_s + E_{pq}\Theta_s)(D_{qp}g\bar{\Lambda}_s + E_{qp}\bar{\Theta}_s). \tag{44}$$

The real parts of λ determine the stability of the solutions. Note Ψ is complex in general.

Combination instabilities of the difference type are examined by letting $s\Omega = \omega_p - \omega_q + \varepsilon\sigma$ ($\omega_p > \omega_q$) where p, $q \leqslant 3$. The λ analogous to Eq. (44) are

$$\lambda = \frac{1}{2}\{-\varsigma(\omega_p+\omega_q) + \mathrm{i}\sigma \pm [\varsigma^2(\omega_p-\omega_q)^2 - \sigma^2 + 2\mathrm{i}\varsigma\sigma(\omega_p-\omega_q) - \Psi]^{1/2}\}. \tag{45}$$

The interaction between rotation modes 1, 2 and 3 in Eq. (14) and translation modes 4 and 5 is examined by letting $s\Omega = \omega_p + \omega_q + \varepsilon\sigma$ ($p < 4$, $q \geqslant 4$). The solvability conditions for Eq. (40) are

$$2\mathrm{i}\omega_p\frac{\partial A_p}{\partial\tau} + 2\mathrm{i}\varsigma\omega_p^2 A_p = 0, \tag{46}$$

$$2\mathrm{i}\omega_q\frac{\partial A_q}{\partial\tau} + 2\mathrm{i}\varsigma\omega_q^2 A_q - gD_{qp}\chi_s\bar{A}_p\mathrm{e}^{\mathrm{i}\sigma\tau} = 0. \tag{47}$$

The nontrivial solutions of Eqs. (46) and (47) are

$$A_p = a_p\mathrm{e}^{-\mathrm{i}\varsigma\omega_p\tau} \quad A_q = a_q\mathrm{e}^{\mathrm{i}(\varsigma\omega_p+\sigma)\tau}. \tag{48}$$

These solutions are always bounded, so there are no combination instabilities between a rotation mode and a translation mode. The same is true for combination instabilities between two translation modes, including for $p = q$. As a result, the following results address interactions between rotation modes 1, 2 and 3.

5. Results and discussion

A single-mesh gear pair with the nominal parameters $\bar{k} = 1.95\times10^8\,\mathrm{N/m}$, $\alpha = 0.6$, $\gamma = 0.28$, $c = 1.5$, $\zeta = 0.001$, $\mu = 0.1$ and $\beta = 0.5\mu$ is examined from this point, where $\mu = 0.1$ is consistent with past studies on gear dynamics [6,16,17]. The dimensionless natural frequencies of the rotation modes are $f_1 = 1.55$, $f_2 = 2.09$ and $f_3 = 5.70$. The natural frequencies of the translation modes are $f_4 = 1.85$ and $f_5 = 2.34$.

5.1. Parametric instability from variable mesh stiffness

Without friction ($\mu = g = 0$), the only parametric excitation is from the mesh stiffness. From Eqs. (44) and (45) in the absence of damping ($\zeta = 0$),

$$\lambda = \frac{1}{2}(\mathrm{i}\sigma \pm \sqrt{\Psi - \sigma^2}) \quad \text{for } s\Omega = \omega_p + \omega_q + \varepsilon\sigma,$$
$$\lambda = \frac{1}{2}(\mathrm{i}\sigma \pm \sqrt{-\Psi - \sigma^2}) \quad \text{for } s\Omega = \omega_p - \omega_q + \varepsilon\sigma,$$
$$\Psi = E_{pq}^2|\Theta_s|^2/(\omega_p\omega_q) > 0. \tag{49}$$

The response for mesh frequencies near sum type instability regions is bounded ($\mathrm{Re}(\lambda) < 0$) when $\sigma^2 \geqslant \Psi$ and unbounded ($\mathrm{Re}(\lambda) > 0$) when $\sigma^2 < \Psi$. Thus, the instability boundaries are $s\Omega = \omega_p + \omega_q \pm \varepsilon(|E_{pq}\Theta_s|/\sqrt{\omega_p\omega_q})$. From Eq. (45), difference type instabilities do not occur because $\mathrm{Re}(\lambda) = 0$ for them.

The primary ($s = 1$) instability intervals for single-mode and sum type instabilities are shown in Fig. 5 for perturbation analysis and the recursive process. These methods agree well even up to $\varepsilon = 0.3$. The largest parametric instability region occurs when mesh frequency is in the boundary of $\Omega = 2\omega_3 \pm \varepsilon|E_{33}\Theta_1|/\omega_3$ because of the maximum mesh strain energy in mode 3, i.e., E_{33} is large. The two-mode instabilities $p = 1$, $q = 3$ and $p = 2$, $q = 3$ have much smaller instability regions because $|E_{13}| \ll |E_{33}|$ and $|E_{23}| \ll |E_{33}|$. With fixed $\varepsilon = 0.1$, the instability interval for primary single-mode instability is from $f_m = 11.2$ to 11.6, where $f_m = \Omega/2\pi$. Fig. 6 shows

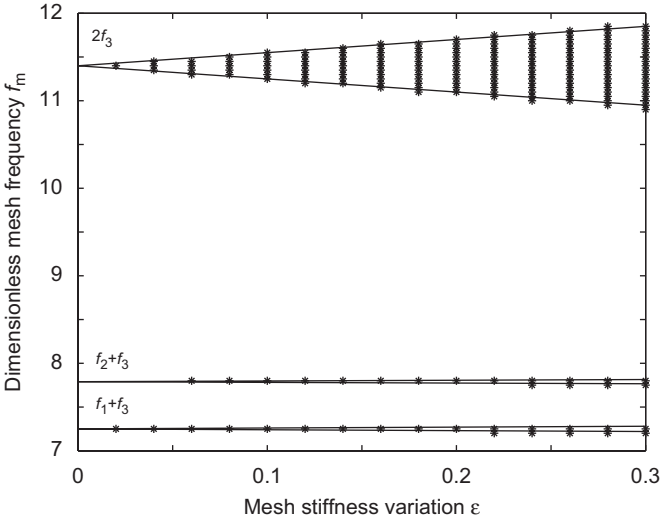

Fig. 5. Instability boundaries for changing dimensionless mesh stiffness variation ε and $\mu = 0$, $\alpha = 0.6$, $\beta = 0$, $c = 1.5$, $\zeta = 0$, $\gamma = 0.28$ (*: recursive process; ——: perturbation).

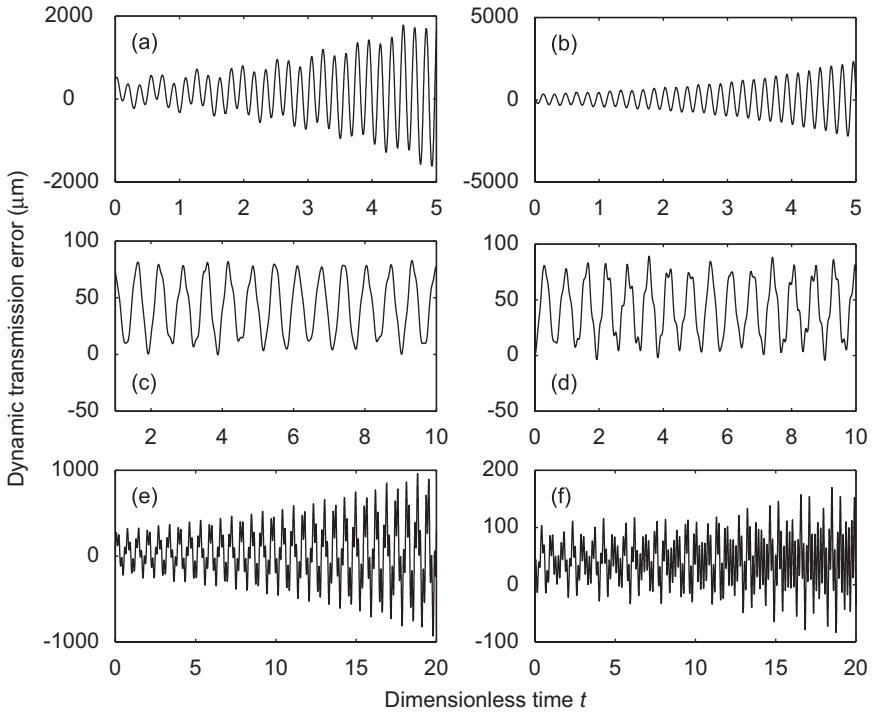

Fig. 6. Dynamic response for dimensionless mesh frequencies near the instability boundaries for $\varepsilon = 0.1$ and other parameters as in Fig. 5: (a) $f_m = 11.2$; (b) $f_m = 11.6$; (c) $f_m = 11.1$; (d) $f_m = 11.7$; (e) $f_m = 7.25$ and (f) $f_m = 7.79$ (all f_m are dimensionless).

linear dynamic responses excited by six mesh frequencies near the instability interval obtained by numerical integration. The amplitudes increase exponentially for $f_m = 11.2$ and 11.6 in Figs. 6a and b. On the other hand, Figs. 6c and d show stable amplitudes for $f_m = 11.1$ and 11.7. The unstable responses at $f_m = 7.25$ and 7.79 for sum type instabilities are shown in Figs. 6e and f, respectively. Therefore, the instability boundary predictions by the recursive process and perturbation approximation agree well with numerical simulation.

5.2. Effect of tooth friction on parametric instability

With friction and damping, the real parts of λ in Eqs. (44) and (45) are

$$\begin{aligned}
&\mathrm{Re}(\lambda) = \frac{1}{2}\left\{-\varsigma(\omega_p+\omega_q) \pm \frac{\sqrt{2}}{2}[(A^2+B^2)^{1/2}+A]^{1/2}\right\},\\
&A = \begin{cases} \varsigma^2(\omega_p-\omega_q)^2 - \sigma^2 + \Psi_R & \text{for } s\Omega = \omega_p+\omega_q+\varepsilon\sigma,\\ \varsigma^2(\omega_p-\omega_q)^2 - \sigma^2 - \Psi_R & \text{for } s\Omega = \omega_p-\omega_q+\varepsilon\sigma, \end{cases}\\
&B = \begin{cases} 2\varsigma\sigma(\omega_p-\omega_q) + \Psi_I & \text{for } s\Omega = \omega_p+\omega_q+\varepsilon\sigma,\\ 2\varsigma\sigma(\omega_p-\omega_q) - \Psi_I & \text{for } s\Omega = \omega_p-\omega_q+\varepsilon\sigma. \end{cases}
\end{aligned} \tag{50}$$

The stability boundaries ($\mathrm{Re}(\lambda)=0$) are determined as $(A^2+B^2)^{1/2}+A = 2\varsigma^2(\omega_p+\omega_q)^2$. Manipulating this yields the boundaries of combination instability with friction as

$$\begin{aligned}
&s\Omega = \omega_p+\omega_q+\frac{1}{8\zeta\omega_p\omega_q}\left[(\omega_p-\omega_q)\Psi_I \pm (\omega_p+\omega_q)\sqrt{\Psi_I^2+16\zeta^2\omega_p\omega_q(\Psi_R-4\zeta^2\omega_p\omega_q)}\right],\\
&s\Omega = \omega_p-\omega_q+\frac{1}{8\zeta\omega_p\omega_q}\left[(\omega_q-\omega_p)\Psi_I \pm (\omega_p+\omega_q)\sqrt{\Psi_I^2+16\zeta^2\omega_p\omega_q(-\Psi_R-4\zeta^2\omega_p\omega_q)}\right],\\
&\Psi_R = \mathrm{Re}(\Psi) = \frac{1}{\omega_p\omega_q}[\varepsilon^2E_{pq}^2|\Theta_s|^2 + \mu^2D_{pq}D_{qp}|\Lambda_s|^2 + \mu\varepsilon E_{pq}(D_{pq}+D_{qp})\mathrm{Re}(\Lambda_s\bar{\Theta}_s)],\\
&\Psi_I = \mathrm{Im}(\Psi) = \frac{\mu\varepsilon}{\omega_p\omega_q}E_{pq}(D_{pq}-D_{qp})\mathrm{Im}(\Lambda_s\bar{\Theta}_s),
\end{aligned} \tag{51}$$

where $\omega_p > \omega_q$ and $\bar{\Theta}_s$ is the complex conjugate of Θ_s.

The effects of mesh stiffness variations and friction bending effect are incorporated in $\varepsilon|\Theta_s|$. The effects of friction moments are included in $\mu|\Lambda_s|$. The difference type instabilities, which are absent for $\mu = 0$, arise when $\mu \neq 0$. Each instability region occurs as a backbone (e.g., $(\omega_p-\omega_q)\Psi_I/8\zeta\omega_p\omega_q$ for sum type instability) and a symmetric deviation (the terms after $\pm$ in Eq. (51)). The backbones are linear functions of μ and ε whose slopes are determined by modal properties, mesh stiffness variations and sliding friction. For the same two modes and the same s, the backbone slopes for the sum and difference type instabilities have equal magnitude and opposite sign. The backbone slopes for the sum type are negative; they are positive for the difference type. The deviations can be approximated as linear functions of μ and ε with Taylor expansion of the square roots.

Fig. 7 shows the instability boundaries varying with μ while the friction bending $\beta = 0$. Mesh frequency f_m varies from 1.7 to 12 covering most combination and single-mode instabilities. The perturbation solutions agree well with numerical solutions. For a combination instability to occur, the corresponding quantity inside the square root of Eq. (51) (call it Δ) must be positive. This quantity Δ, which also governs the width of the instability region, depends on strength of parametric excitation, friction, modal mesh strain energy (as captured by E_{pq} and D_{pq}), natural frequency and damping. For fixed system parameters, the modal mesh strain energy dictates existence and width of a possible instability. For instance, sum type instability for modes 1, 2 does not occur because $\Delta = -1.6\times10^{-5} < 0$. Sum type instabilities involving modes 1, 3 and modes 2, 3 are present because $\Delta = 0.0014$ and 0.0009, respectively, a result of the larger modal mesh strain energy in mode 3. The instability intervals for modes 1, 3 are larger than for modes 2, 3 for the same type of instability (sum or difference) because mode 1 has stronger mesh strain energy than mode 2. Note that in the absence of

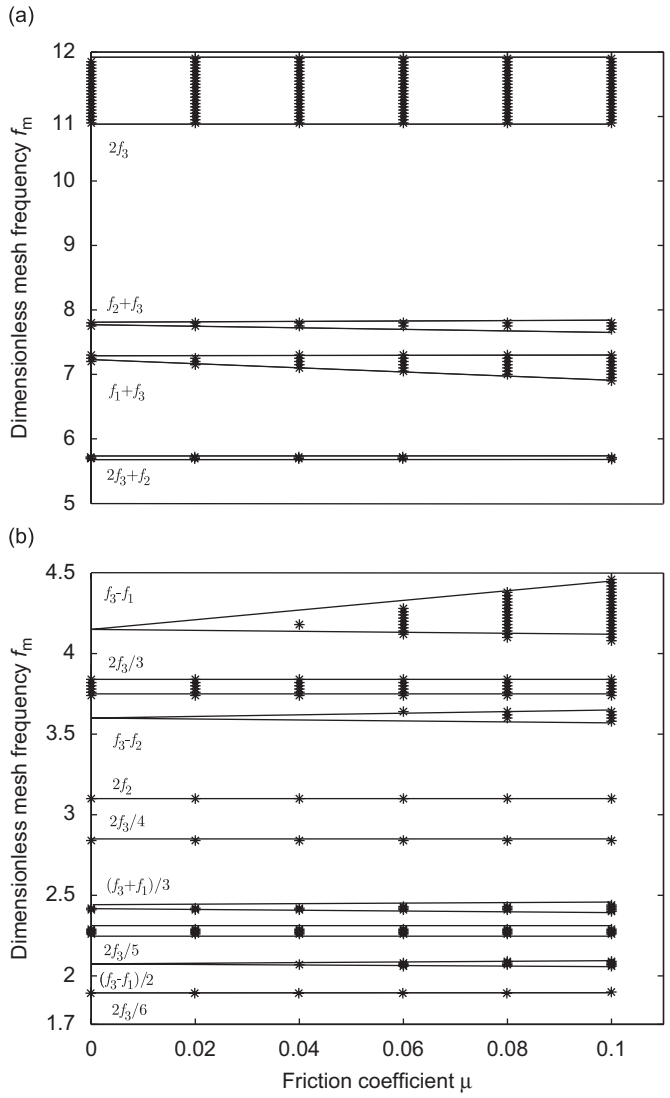

Fig. 7. Instability boundaries for changing dimensionless friction coefficient μ and $\alpha = 0.6$, $\beta = 0$, $\varepsilon = 0.3$, $c = 1.5$, $\zeta = 0.001$, $\gamma = 0.28$ (*: recursive process; ——: perturbation): (a) f_m from 1.7 to 4.5 and (b) f_m from 5 to 12.

damping $\Delta > 0$ and instability always occurs. In essence, there is a critical mesh strain energy required to overcome the damping and create instability.

The sum type instability intervals (i.e., deviations) are larger than the difference type for the same two modes, as proved in Appendix B. The sum type instability occurs even when $\mu = 0$ and is more sensitive to μ and ε than the difference type. The widths of the two-mode instability boundaries (sum and difference types) increase almost linearly with μ.

For single-mode instabilities ($p = q$), $\Psi_I = 0$ and the instability boundaries simplify to

$$s\Omega = 2\omega_p \pm \sqrt{|\varepsilon E_{pp}\Theta_s + \mu D_{pp}\Lambda_s|^2/\omega_p^2 - 4\zeta^2\omega_p^2}. \tag{52}$$

The backbones vanish, in contrast to the two-mode instabilities. The instability intervals depend on $\varepsilon\Theta_s$ (mesh stiffness variation and friction bending) and $\mu\Lambda_s$ (friction moments). In practice, $\varepsilon > \mu$, $E_{pp} > D_{pp}$ and $|\Theta_s| > |\Lambda_s|$ due to the moment arm of friction l_i being less than the base radius. Thus, $|\varepsilon E_{pp}\Theta_s| \gg |\mu D_{pp}\Lambda_s|$ and the single-mode instabilities are sensitive to the friction bending effect and mesh stiffness variations while less

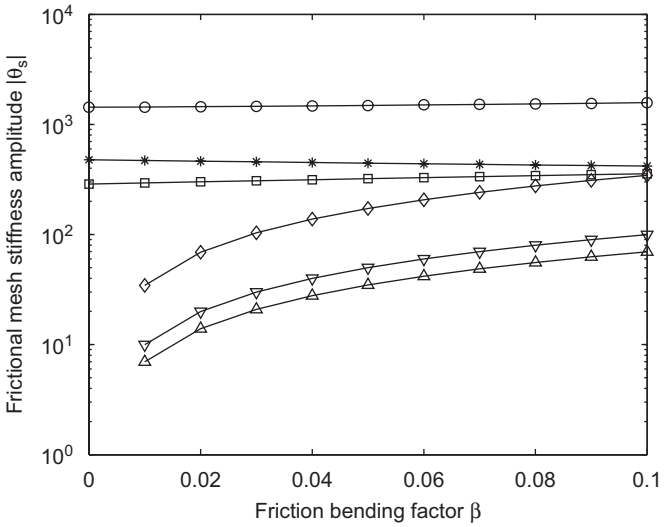

Fig. 8. Effect of dimensionless friction bending ratio β on the dimensionless mesh stiffness. Fourier harmonics Θ_s for $\alpha = 0.6$, $\varepsilon = 0.3$, $c = 1.5$, $\gamma = 0.28$ ($\circ$: $s = 1$, $\diamond$: $s = 2$, *:$s = 3$, Δ: $s = 4$, $\square$: $s = 5$, ∇: $s = 6$).

sensitive to friction moments as evident in Fig. 7. Because $|E_{33}| \gg |E_{11}| > |E_{22}|$, primary instabilities of modes 1 and 3 emerge in Fig. 7, and the interval of mode 3 is much larger than that of mode 1. Higher order instabilities ($s = 1, 2, \ldots, 6$) also exist for mode 3. The intervals for odd order ($s = 1,3,5$) are larger than for even order ($s = 2,4,6$) because, for rectangular wave mesh stiffness, odd harmonics have higher magnitudes than even harmonics (Fig. 8).

5.3. Effect of friction bending on parametric instability

The effects of friction bending ratio β on the mesh stiffness harmonics Θ_s are shown in Fig. 8. Given $\varepsilon = 0.3$, $c = 1.5$, $\alpha = 0.6$ and $\gamma = 0.26$, the odd order harmonics are not sensitive to β while the even order harmonics are. As a result, the instability intervals with odd s are insensitive to β while those with even s are sensitive to β. As illustrated in Fig. 9, the intervals with $s = 1,3,5$ are almost independent of β. The instabilities with $s = 2$, 4, 6, such as, $sf_m \approx 2f_3$ ($s = 2$, 4, 6) and $sf_m \approx f_3 - f_1$ ($s = 2$), however, change with β. The single-mode instabilities for $p = q = 3$ exist even for $s = 2$, 4, 6 because the third mode has the maximum mesh strain energy even though the $|\Theta_{2,4,6}|$ are much smaller than $|\Theta_1|$. For $p = q = 3$, the single-mode instability intervals with $s = 2$, 4, 6 are increased by the bending ratio β, while the intervals for $s = 4$, 6 are much smaller than for $s = 2$ (note different scales in two graphs) because $|\Theta_4| < |\Theta_6| < |\Theta_2|$ in Fig. 8.

5.4. Effect of contact ratio on parametric instability

The contact ratio c affects both Λ_s and Θ_s (i.e., the harmonics of parametric excitation included in Ψ of Eq. (51)), so the impact of contact ratio on instability boundaries changes with tooth friction. Fig. 10 shows the effect of contact ratio on single-mode and two-mode sum type instabilities with tooth friction and bending effect. The sum type instability boundaries without tooth friction are

$$\Omega = \omega_p + \omega_q \pm \frac{(\omega_p + \omega_q)}{2\omega_p\omega_q}\sqrt{\varepsilon^2|E_{pq}\tilde{\Theta}_s|^2 - 4\zeta^2\omega_p^2\omega_q^2}, \tag{53}$$

where the harmonics of frictionless mesh stiffness are

$$\tilde{\Theta}_s = \frac{\bar{k}}{s\pi}\sin s\pi(c-1)[\cos s\pi(c-1+2\gamma) + \mathrm{i}\sin s\pi(c-1+2\gamma)]. \tag{54}$$

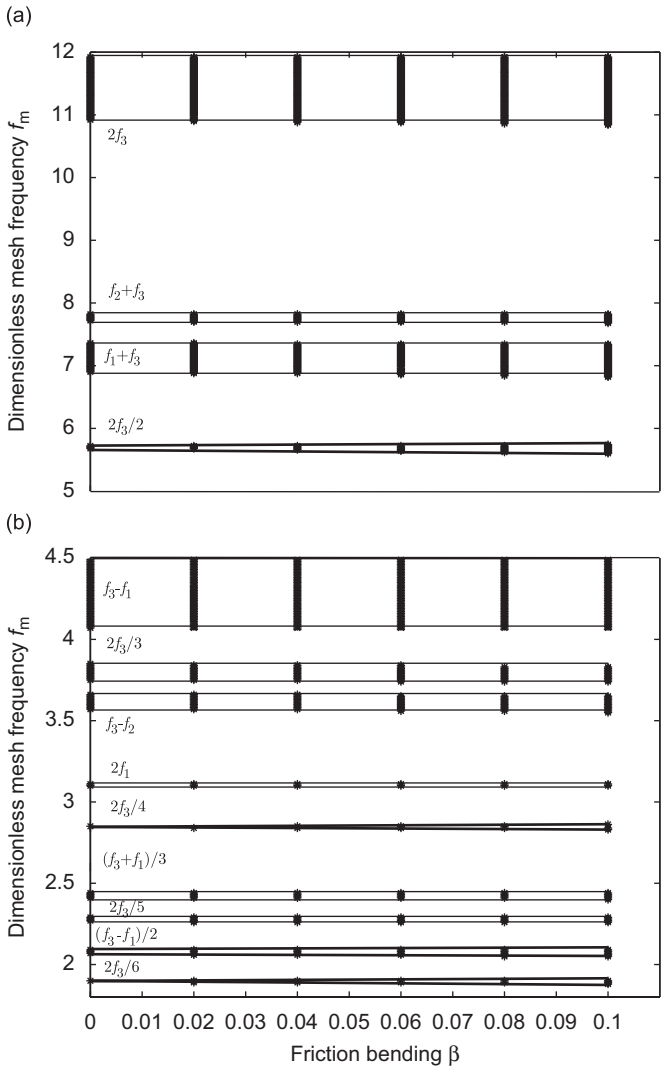

Fig. 9. Instability boundaries for changing dimensionless friction bending β and $\alpha = 0.6$, $\mu = 0.1$, $c = 1.5$, $\varepsilon = 0.3$, $\zeta = 0.001$, $\gamma = 0.28$ (*: recursive process; ——: perturbation): (a) f_m from 1.7 to 4.5 and (b) f_m from 5 to 12.

Without tooth friction, the instability boundaries for varying contact ratio have sinusoidal profiles symmetric about $c = 1.5$ as $|\tilde{\Theta}_s| = \bar{k}|\sin s\pi(c-1)|/(s\pi)$, and the number of waves for each profile depends on s.

The instability boundaries with friction shown in Fig. 10 are calculated by the perturbation and numerical recursive methods. The boundaries do not have sinusoidal profiles. The two-mode instabilities are determined by the complicated functions of Ψ_R and Ψ_I in Eq. (51) that are affected by the contact ratio c, friction moment μ, and friction bending β. The boundaries of two-mode instabilities are sensitive to μ, and the boundaries of single-mode instabilities for even s are sensitive to β. The sum type instability boundaries shown in Fig. 10 are no longer symmetric about $c = 1.5$. The contact ratio having maximum boundary width is shifted to lower c due to tooth friction. The instability intervals with tooth friction are greater than those without friction because of the increased excitation. The secondary instability ($s = 2$) at f_3 occurs even for $c = 1$ due to the sensitivity to friction bending. The influence of contact ratio on the primary instability at $2f_3$ is minimal because that instability is insensitive to friction moment and bending effect as shown previously. The profile of the primary instability in Fig. 10 is almost a symmetric sinusoidal profile even with friction.

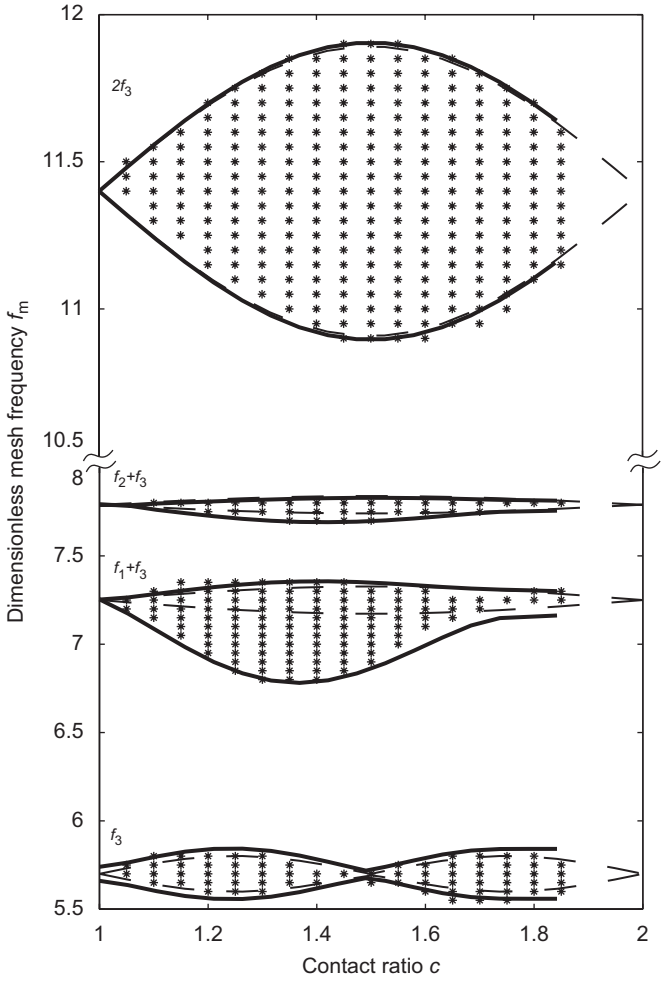

Fig. 10. Influence of contact ratio on parametric instability boundaries for $\alpha = 0.6$, $\mu = 0.1$, $\beta = 0.05$, $\varepsilon = 0.3$, $\zeta = 0.001$, $\gamma = 0.05$ (- - - perturbation $\mu = 0$; —— perturbation $\mu = 0.1$; * numerical $\mu = 0.1$).

Note that $c-1+\gamma \leqslant 1$ is required according to Fig. 2. The analytical and numerical results for $c \geqslant 2-\gamma = 1.85$ with the selected $\gamma = 0.15$ have no physical meaning.

5.5. *Effect of modal damping on parametric instability*

From Eqs. (51) and (52), the instability boundaries decrease with an increase in modal damping. Different types of instabilities have different critical damping where the unstable interval vanishes. Fig. 11 shows the influence of damping on single-mode and two-mode combination instabilities. The perturbation and numerical solutions agree well. The primary single-mode instability has the biggest critical damping due to the strongest mesh strain energy in mode 3. The other instabilities decrease more rapidly than for the primary single-mode. The f_1+f_3 combination instability has greater critical modal damping compared to the f_2+f_3 combination due to the higher mesh strain energy of mode 1 than mode 2. The critical modal damping depends on tooth friction, mesh stiffness variation and contact ratio.

5.6. *Influence of tooth friction on dynamic response*

The parameters of two practical gears listed in Table 1 are used to generate finite element gear models. For comparison purposes, the realistic mesh stiffness variations over a mesh cycle calculated from the finite

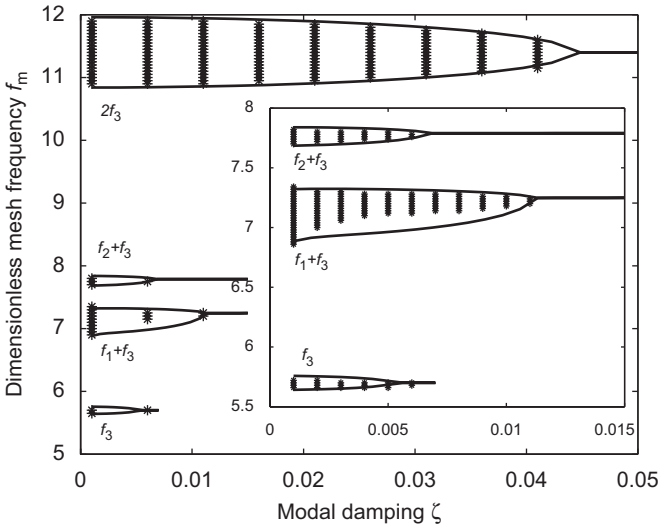

Fig. 11. Impact of modal damping on instability boundaries for $\alpha = 0.6$, $\mu = 0.1$, $\beta = 0.05$, $\gamma = 0.28$, $c = 1.5$, $\varepsilon = 0.3$ (—— perturbation; * numerical method).

element model are used as the frictionless mesh stiffness in the analytical model. The mesh parameters are $\bar{k} = 2.98\text{e}8\,\text{N/m}$, $T_1 = 100\,\text{N m}$, $\mu = 0.1$, $c = 1.4$ and $\zeta = 0.02$. The friction bending effect is inherently included in the finite element analysis. The bending factor β used in the analytical model is estimated from Eq. (4) where the deflection and load are calculated from finite element static analysis.

The parametric instabilities for two-mode and single-mode combinations result in exponentially growing dynamic response, which eventually triggers nonlinear contact loss. The nonlinearity suppresses the growth of the amplitude and usually yields a steady periodic response. To study the sensitivity of nonlinear response on tooth friction and validate the proposed analytical model, numerical simulations of the nonlinear analytical model in Eq. (13) and the finite element model are compared in Fig. 12a. Fig. 12b shows the spectral details. Decreasing speed sweep analyses are conducted to cover the frequency range that includes the fundamental resonance of rotational mode 1 at $f_1 = 1835\,\text{Hz}$ and higher harmonic resonances of rotational mode 3 at $f_3 = 6924\,\text{Hz}$. The root-mean-square values of the dynamic transmission error u are calculated by

$$u_{\text{rms}} = \left[\frac{1}{nT}\int_0^{nT} (u-\bar{u})^2\,\mathrm{d}t\right]^{1/2}, \tag{55}$$

where $\bar{u}$ is the mean value of u. The analytical models with and without friction bending effect agree well with the finite element model in Fig. 12a for the resonances at 1731 and 1835 Hz where the fourth harmonic excites mode 3 (Fig. 12b) and the first harmonic excites mode 1, respectively. Tooth friction has negligible effect on these two single-mode resonances and in the off-resonant frequency ranges.

The finite element results reveal that tooth friction significantly excites the resonance at 2308 Hz where the third harmonic ($s = 3$) excites mode 3 as shown in Fig. 12b. The analytical model with friction bending effect shows a similar strong influence of tooth friction on this resonance. The analytical result for $\mu = 0.1$ and $\beta = 0$, which ignores the friction bending effect, cannot capture the strong impact of tooth friction on this resonance. This implies that the friction bending effect plays a key role in exciting this higher harmonic resonance. These findings confirm the conclusions from the stability analysis.

6. Conclusions

A translational–rotational model with parametric excitations from variable mesh stiffness, tooth sliding friction moments, and a heretofore unexamined friction bending effect is established for a single-mesh gear

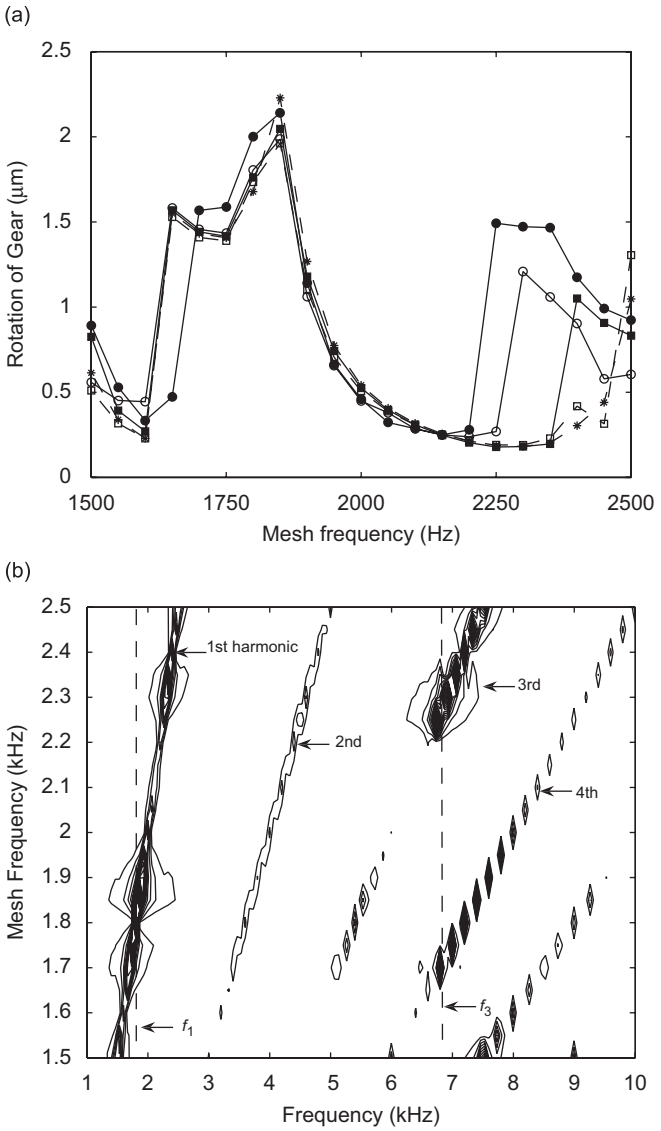

Fig. 12. Speed sweep analysis for $\alpha = 0.6$, $\gamma = 0.28$, $c = 1.4$, $\varepsilon = 0.28$, $\zeta = 0.02$: (a) root-mean-square comparisons (■: finite element $\mu = 0$; □: analytical $\mu = 0$; ●: finite element $\mu = 0.1$; ○: analytical $\mu = 0.1$, $\beta = 0.05$; *: analytical $\mu = 0.1$, $\beta = 0$) and (b) finite element Campbell diagram $\mu = 0.1$.

pair. A numerical recursive method based on Floquet theory and a perturbation analysis examines the associated parametric instabilities and show strong agreement. The analytical expressions for instability boundaries reveal how key parameters impact the instabilities. The nonlinear responses from the analytical model and a finite element benchmark also agree even when contact loss occurs.

1. Combination instabilities between a rotation mode and a translation mode or two translation modes cannot occur. Sum type and single-mode instabilities can occur for both frictional and frictionless conditions. Difference type instabilities occur only when friction is present.
2. Two-mode combination instabilities are sensitive to the friction moment and bending effect. Single-mode instabilities are insensitive to the friction moment but sensitive to the friction bending effect. The instability interval widths depend nearly linearly on mesh stiffness variations.

3. For the same type of instabilities, the instability intervals for different modes depend on the total mesh strain energy of the mode or the modes in combination. The mesh strain energy needs to be over a critical value to cause the instability. The sum type instability intervals are larger than for the difference type.
4. The effects of contact ratio on the instability intervals of two-mode combination and single-mode instabilities are altered significantly by the friction moments and the friction bending effect, respectively. The tooth friction destroys symmetry of the instability boundaries for varying contact ratio. The friction bending can cause instability even for integer contact ratios.
5. The proposed analytical model agrees with a finite element benchmark for nonlinear response due to parametric instabilities, while the model without considering friction bending fails to predict the strong influence of tooth friction on certain parametric instabilities. The nonlinear dynamic analyses confirm that the friction bending effect can significantly alter the vibration.

Appendix A. Expansion of terms in Eq. (18)

$$L_{1,0} = -\mu\kappa_1\bar{k}\frac{\eta\rho_0 r_2 + r_1(1-\eta)(D-\rho_0)}{r_1 r_2}, \quad L_{1,1} = -\mu\kappa_1\bar{k}\Omega\frac{\eta r_2 - r_1(1-\eta)}{r_2}, \tag{A.1}$$

$$\begin{aligned}
L_{2,0} &= \frac{\mu\bar{k}}{r_1 r_2}\{r_1(1-\eta)[\kappa_3(D-\rho_1+2\pi r_1)-\kappa_2(D-\rho_1)] + r_2\eta[\kappa_3(\rho_1-2\pi r_1)-\kappa_2\rho_1]\},\\
L_{2,1} &= \frac{\mu\bar{k}\Omega}{r_2}[r_2\eta + r_1(1-\eta)](\kappa_3-\kappa_2) + \frac{2\mu w}{r_1 r_2}[r_2\eta(\rho_1-\pi r_1) + r_1(1-\eta)(D-\rho_1+\pi r_1)],\\
L_{2,2} &= \frac{2\mu w\Omega}{r_2}[(1-\eta)r_1 - \eta r_2],
\end{aligned} \tag{A.2}$$

$$L_{3,0} = \mu\kappa_4\bar{k}\frac{\eta\rho_2 r_2 + r_1(1-\eta)(D-\rho_2)}{r_1 r_2}, \quad L_{3,1} = \mu\kappa_4\bar{k}\Omega\frac{\eta r_2 - r_1(1-\eta)}{r_2}. \tag{A.3}$$

Appendix B. Proof of instability deviation relation

Examination of Eq. (51) shows that proving the deviation of a sum type instability is larger than for the difference type is achieved by showing $\Psi_R \geqslant 0$. To begin, consider the first component equation of the eigenvalue problem $\bar{\mathbf{K}}\phi_p = \omega_p^2\mathbf{M}\phi_p$, which gives the following relations between the modal deflections:

$$\phi_{p3} - \phi_{p5} = \frac{J_e\omega_p^2 - \bar{k}}{\bar{k}}\phi_{p1} \Rightarrow \phi_{p1}(\phi_{p1} + \phi_{p3} - \phi_{p5}) = \frac{J_e\omega_p^2}{\bar{k}}\phi_{p1}^2 > 0. \tag{B.1}$$

From Eqs. (14), (32) and (B.1),

$$D_{pq}D_{qp} = \phi_{p1}\phi_{q1}(\phi_{p1}+\phi_{p3}-\phi_{p5})(\phi_{q1}+\phi_{q3}-\phi_{q5}) = \left(\frac{J_e\omega_p\omega_q}{\bar{k}}\phi_{p1}\phi_{q1}\right)^2 > 0. \tag{B.2}$$

This implies D_{pq} and D_{qp} have the same sign. The following is for positive D_{pq} and D_{qp}, with straightforward modification for negative values. From $(D_{pq}-D_{qp})^2 \geqslant 0$,

$$\left|D_{pq} + D_{qp}\right| \geqslant 2\sqrt{D_{pq}D_{qp}}. \tag{B.3}$$

The Fourier coefficients in Eq. (30) are expressed in real and imaginary parts as

$$\left.\begin{aligned}\Lambda_s &= \Lambda_R + \mathrm{i}\Lambda_I\\ \Theta_s &= \Theta_R + \mathrm{i}\Theta_I\end{aligned}\right\} \Rightarrow \mathrm{Re}(\Lambda_s\bar{\Theta}_s) = \Lambda_R\Theta_R + \Lambda_I\Theta_I. \tag{B.4}$$

From Eqs. (51), (B.3) and (B.4),

$$\Psi_R = \frac{1}{\omega_p \omega_q}(\Psi_{R1} + \Psi_{R2}), \tag{B.5}$$

$$\begin{aligned}
\Psi_{R1} &= \varepsilon^2 E_{pq}^2 \Theta_R^2 + \mu^2 D_{pq} D_{qp} \Lambda_R^2 + \mu\varepsilon E_{pq}(D_{pq} + D_{qp})\Lambda_R \Theta_R \geqslant \left(\varepsilon E_{pq}\Theta_R + \mu\sqrt{D_{pq}D_{qp}}\Lambda_R\right)^2 \geqslant 0,\\
\Psi_{R2} &= \varepsilon^2 E_{pq}^2 \Theta_I^2 + \mu^2 D_{pq} D_{qp} \Lambda_I^2 + \mu\varepsilon E_{pq}(D_{pq} + D_{qp})\Lambda_I \Theta_I \geqslant \left(\varepsilon E_{pq}\Theta_I + \mu\sqrt{D_{pq}D_{qp}}\Lambda_I\right)^2 \geqslant 0.
\end{aligned} \tag{B.6}$$

Combination of Eqs. (B.5) and (B.6) yields $\Psi_R \geqslant 0$.

References

[1] H.N. Ozguven, D.R. Houser, Mathematical-models used in gear dynamics-a review, *Journal of Sound and Vibration* 121 (1988) 383–411.

[2] G.W. Blankenship, R. Singh, A comparative study of selected gear mesh force interface dynamic models, *ASME Sixth Power Transmission and Gearing Conference*, Paper No. DE-43-1, Phoenix, AZ, September 1992.

[3] J. Wang, R. Li, X. Peng, Survey of nonlinear vibration of gear transmission systems, *ASME Applied Mechanics Review* 56 (2003) 309–329.

[4] H.N. Ozguven, D.R. Houser, Dynamic analysis of high-speed gears by using loaded static transmission error, *Journal of Sound and Vibration* 125 (1988) 71–83.

[5] J. Lin, R.G. Parker, Mesh stiffness variation instabilities in two-stage gear systems, *Journal of Vibration and Acoustics* 124 (2002) 68–76.

[6] P. Velex, V. Cahouet, Experimental and numerical investigations on the influence of tooth friction in spur and helical gear dynamics, *Journal of Mechanical Design* 122 (2000) 515–522.

[7] J. Borner, D.R. Houser, Friction and bending moments on gear noise excitations, *SAE Transaction* 105 (1996) 1669–1676.

[8] D.R. Houser, V.M. Bolze, J.M. Graber, Static and dynamic transmission error measurements and predictions for spur and helical gear sets, *Proceedings of the Seventh ASME International Power Transmission and Gearing Conference*, San Diego, CA, October 1996, pp. 365–372.

[9] M. Vaishya, D.R. Houser, Modeling and analysis of sliding friction in gear dynamics, *Proceedings of the Eighth ASME International Power Transmission and Gearing Conference*, Baltimore, MD, September 2000, pp. 601–610.

[10] K.F. Martin, A review of friction predictions in gear teeth, *Wear* 49 (1978) 201–238.

[11] B.W. Kelley, A.J. Lemanski, Lubrication of involute gearing, *Proceedings of Institution of Mechanical Engineers* 182 (1967) 173–184.

[12] S. Wu, H.S. Cheng, A friction model of partial-EHL contacts and its application to power loss in spur gears, *Tribology Transaction* 34 (1991) 397–407.

[13] B. Rebbechi, F.B. Oswald, D.P. Townsend, Measurement of gear tooth dynamic friction, *Proceedings of the Seventh ASME international Power Transmission and Gearing Conference*, San Diego, CA, October 1996, pp. 355–363.

[14] S. He, R. Gunda, R. Singh, Effect of sliding friction on the dynamics of spur gear pair with realistic time-varying stiffness, *Journal of Sound and Vibration* 301 (2007) 927–949.

[15] O. Lundvall, N. Stromberg, A. Klarbring, A flexible multi-body approach for frictional contact in spur gears, *Journal of Sound and Vibration* 278 (2004) 479–499.

[16] M. Vaishya, R. Singh, Analysis of periodically varying gear mesh systems with coulomb friction using Floquet theory, *Journal of Sound and Vibration* 243 (2001) 525–545.

[17] M. Vaishya, R. Singh, Sliding friction-induced non-linearity and parametric effects in gear dynamics, *Journal of Sound and Vibration* 248 (2001) 671–694.

[18] R. Gunda, R. Singh, Dynamic analysis of sliding friction in a gear pair, *ASME 2003 Design Engineering Technical Conferences and Computers and Information in Engineering Conference*, Paper No. PTG 48055, Chicago, IL, September 2–6, 2003.

[19] H. Iida, A. Tamura, Y. Yamada, Vibrational characteristics of friction between gear teeth, *Bulletin of JSME* 28 (1985) 1512–1519.

[20] D. Hochmann, Friction Force Excitations in Spur and Helical Involute Parallel Axis Gearing, PhD Dissertation, The Ohio State University, 1997.

[21] G.V. Tordion, R. Gauvin, Dynamic stability of a two-stage gear train under the influence of variable meshing stiffnesses, *ASME Journal of Engineering Industry* 99 (1977) 785–791.

[22] J.G. Bollinger, R.J. Harker, Instability potential of high speed gearing, *Journal of the Industrial Mathematics* 17 (1967) 39–55.

[23] C. Nataraj, A.M. Whitman, Parameter excitation effects in gear dynamics, *The 16th ASME Design Engineering Technical Conferences*, Paper No. DETC97/VIB-4018, Sacramento, CA, September 1997.

[24] M. Benton, A. Seireg, Factors influencing instability and resonances in geared systems, *Journal of Mechanical Design* 103 (1981) 372–378.

[25] J. Lin, R.G. Parker, Parametric instability of planetary gears under mesh stiffness variation, *Journal of Sound and Vibration* 29 (2002) 411–429.

[26] S. He, R. Singh, Dynamic interactions between sliding friction and tip relief in spur gears, *ASME Design Engineering Technical Conferences*, Paper No. PTG 34077, Las Vegas, NV, September 2007.
[27] C. Lee, H.H. Lin, F.B. Oswald, D.P. Townsend, Influence of linear profile modification and loading conditions on the dynamic tooth load and stress of high-contact-ratio spur gears, *Journal of Mechanical Design* 113 (1991) 473–480.
[28] R.G. Parker, S.M. Vijayakar, T. Imajo, Nonlinear dynamic response of a spur gear pair: Modeling and experimental comparisons, *Journal of Sound and Vibration* 237 (2000) 435–455.
[29] R.G. Parker, V. Agashe, S.M. Vijayakar, Dynamic response of a planetary gear system using a finite element/contact mechanics model, *Journal of Mechanical Design* 122 (2000) 304–310.
[30] E.I. Butikov, Parametric excitation of a linear oscillator, *European Journal of Physics* 25 (2004) 535–554.
[31] J.A. Richards, *Analysis of Periodically Time-Varying Systems*, Springer, New York, 1983.
[32] R.E. Barterls, A time integration algorithm based on the state transition matrix for structures with time varying and nonlinear properties, *Computers and Structures* 81 (2003) 349–357.
[33] T. Kucharski, A method for dynamic response analysis of time-varying discrete systems, *Computers and Structures* 76 (2000) 545–550.
[34] C.S. Hsu, W.H. Cheng, Applications of the theory of impulsive parametric excitation and new treatments of general parametric excitation problems, *Journal of Applied Mechanics* 40 (1973) 78–86.
[35] P. Friedmann, C.E. Hammond, T. Woo, Efficient numerical treatment of periodic systems with application to stability problems, *International Journal for Numerical Methods in Engineering* 11 (1977) 1117–1136.
[36] C.S. Hsu, Impulsive parametric excitation: theory, *Journal of Applied Mechanics* 39 (1972) 551–558.